ANL-AFCI-186

Preliminary Validation Studies of Existing Neutronics Analysis Tools for Advanced Burner Reactor Design Applications

Nuclear Engineering Division

About Argonne National Laboratory
Argonne is a U.S. Department of Energy laboratory managed by UChicago Argonne, LLC under contract DE-AC02-06CH11357. The Laboratory's main facility is outside Chicago, at 9700 South Cass Avenue, Argonne, Illinois 60439. For information about Argonne and its pioneering science and technology programs, see www.anl.gov.

DOCUMENT AVAILABILITY

Online Access: U.S. Department of Energy (DOE) reports produced after 1991 and a growing number of pre-1991 documents are available free at OSTI.GOV (http://www.osti.gov/), a service of the US Dept. of Energy's Office of Scientific and Technical Information.

Reports not in digital format may be purchased by the public from the National Technical Information Service (NTIS):
U.S. Department of Commerce
National Technical Information Service
5301 Shawnee Rd
Alexandria, VA 22312
www.ntis.gov
Phone: (800) 553-NTIS (6847) or (703) 605-6000
Fax: (703) 605-6900
Email: **orders@ntis.gov**

Reports not in digital format are available to DOE and DOE contractors from the Office of Scientific and Technical Information (OSTI):
U.S. Department of Energy
Office of Scientific and Technical Information
P.O. Box 62
Oak Ridge, TN 37831-0062
www.osti.gov
Phone: (865) 576-8401
Fax: (865) 576-5728
Email: **reports@osti.gov**

Disclaimer
This report was prepared as an account of work sponsored by an agency of the United States Government. Neither the United States Government nor any agency thereof, nor UChicago Argonne, LLC, nor any of their employees or officers, makes any warranty, express or implied, or assumes any legal liability or responsibility for the accuracy, completeness, or usefulness of any information, apparatus, product, or process disclosed, or represents that its use would not infringe privately owned rights. Reference herein to any specific commercial product, process, or service by trade name, trademark, manufacturer, or otherwise, does not necessarily constitute or imply its endorsement, recommendation, or favoring by the United States Government or any agency thereof. The views and opinions of document authors expressed herein do not necessarily state or reflect those of the United States Government or any agency thereof, Argonne National Laboratory, or UChicago Argonne, LLC.

ANL-AFCI-186

Preliminary Validation Studies of Existing Neutronics Analysis Tools for Advanced Burner Reactor Design Applications

prepared by
W. S. yang, T. K. Kim, S. J. Kim, and C. H. Lee
Nuclear Engineering Division, Argonne National Laboratory

April 30, 2007

Advanced Fuel Cycle Initiative	**DOCUMENT RELEASE AUTHORIZATION**	

Argonne National Laboratory
9700 South Cass Avenue
Argonne, IL 60439

ANL AFCI Document Number:	ANL-AFCI-186	Release Date:	4/30/207

Title:	Preliminary Validation Studies of Existing Neutronics Analysis Tools for Advanced Burner Reactor Design Applications
Author(s):	W. S. Yang, T. K. Kim, S. J. Kim, and C. H. Lee

Approval for Release

Approved by:			Date
Principal Author	Won Sik Yang	Won Sik Yang	4/30/07
ANL Work Package Manager	Robert N. Hill	Robert N. Hill	4/30/07
ANL Program Manager	Robert N. Hill	Robert N. Hill	4/30/07

Intentional blank

ANL-AFCI-186

Preliminary Validation Studies of Existing Neutronics Analysis Tools for Advanced Burner Reactor Design Applications

W. S. Yang, T. K. Kim, S. J. Kim, and C. H. Lee

Nuclear Engineering Division

9700 South Cass Avenue

Argonne National Laboratory

Argonne, IL 60439

April 30, 2007

Table of Contents

Executive Summary 1

1. Introduction 3

2. Numerical Benchmark Analysis of 250 MWt ABTR 5

2.1 Description of ABTR Benchmark Problem 5

2.2 Cross Section Generation 6

2.3 Analysis Methods 8

2.4 Results 11

2.4.1 Core Multiplication Factor 11

2.4.2 Nuclear Data Effects 14

2.4.3 Local Heterogeneity Effects 15

2.4.4 Sodium Void Worth 17

2.4.5 Control Assembly Worth 18

2.4.6 Isothermal Temperature Coefficients 20

2.4.7 Assembly Power Distribution 20

2.4.8 Effects of Anisotropic Scattering Correction and Refined Resonance Absorption 21

3. Analysis of ZPPR-21 Critical Experiment Benchmarks 23

3.1 Description of ZPPR-21 Critical Experiments 23

3.2 Cross Section Generation 26

3.3 Reference VIM Monte Carlo Calculations 26

3.4 TWODANT Core Calculation 27

3.4.1 Effect of Scattering Order and Angular Quadrature 27

3.4.2 Effect of Anisotropic Scattering Cross Section Correction 28

3.4.3 Transport Effect 29

3.4.4 Core-Reflector Interface Effect 31

3.5 Verification of MC^2-2/TWODANT against VIM Monte Carlo Calculation 32

3.6 Validation of MC^2-2/TWODANT against Benchmark Experimental Values.....37
3.7 Group Collapsing Methods.....38
4. Preliminary Tests of ENDF/B-VII Data.....41
5. Conclusions.....46
References.....48
Appendix A. ABTR Numerical Benchmark Problem.....50

List of Tables

Table 2.1 Cross Section Libraries Used in MCNP5 Calculations 9

Table 2.2 Core Multiplication Factors from MCNP5 Calculations 11

Table 2.3 Core Multiplication Factors from Nodal Transport Calculations 12

Table 2.4 Core Multiplication Factors from Nodal Diffusion Calculations 12

Table 2.5 Difference in Core Multiplication Factor (pcm Δk) between VARIANT Nodal Transport and MCNP5 Monte Carlo Solutions 13

Table 2.6 Transport and Neutron Energy Group Effects 14

Table 2.7 Core Multiplication Factor Variation by Different Fe and Zr Cross Sections 15

Table 2.8 Total Local Heterogeneity Effects (pcm Δk) 16

Table 2.9 Pin and Duct Heterogeneity Effects of Fuel Assembly (pcm Δk) 17

Table 2.10 Pin and Duct Heterogeneity Effects of Control Assembly (pcm Δk) 17

Table 2.11 Sodium Void Worth ($) 18

Table 2.12 Control Assembly Worth from MCNP5 Calculations ($) 19

Table 2.13 Control Assembly Worth from Deterministic Calculations ($) 19

Table 2.14 Isothermal Temperature Coefficient (¢/K) 20

Table 2.15 Effects of Within-group Scattering Cross Section Correction and Hyper-Fine-Group Resonance Calculation 22

Table 3.1 Principal Mass Loadings in the ZPPR-21 Cores (kg) 23

Table 3.2 Reference Configuration Data for ZPPR-21 24

Table 3.3 k_{eff} Results for ZPPR-21 Phases A through F from VIM Calculations 26

Table 3.4 TWODANT (S24) k_{eff} Values of ZPPR-21 Cores vs. Anisotropic Scattering Order 27

Table 3.5 TWODANT k_{eff} Values of ZPPR-21 Cores vs. Angular Quadrature Order....28

Table 3.6 TWODANT (P5S24) k_{eff} Values of ZPPR-21 Cores vs. Anisotropic Within-Group Scattering Cross Section Correction 28

Table 3.7 Comparison of k_{eff} Values of ZPPR-21 Cores Obtained from TWODANT Transport and DIF3D Diffusion Theory Calculations 29

Table 3.8 Comparison of Leakage Fraction and Main Reaction Rates between TWODANT Transport and DIF3D Diffusion Theory Solutions for ZPPR-21 Cores 30

Table 3.9 Comparison of Leakage Fraction and Main Reaction Rates between TWODANT P1S16 and DIF3D Diffusion Theory Solutions vs. Core Size (ZPPR-21A Compositions) 30

Table 3.10 Reactivity Effects (pcm) of Deviations of TWODANT One-Group Cross Sections from VIM Result (ZPPR-21 Phase A through C) 33

Table 3.11 Reactivity Effects (pcm) of Deviations of TWODANT One-Group Cross Sections from VIM Results (ZPPR-21 Phase D through F) 34

Table 3.12 Comparison of TWODANT k_{eff} Results with Benchmark Values 37

Table 3.13 k_{eff} Results of ZPPR-21 Cores Obtained with Different Group Collapsing Methods 38

Table 4.1 Resonance Data (ENDF/B-VII.0) of Isotopes Used in the ABTR Benchmark 42

Table 4.2 Comparison of Multiplication Factors of Fast System Benchmarks Obtained with ENDF/B-V.2 and ENDF/B-VI.5 Data 44

Table 4.3 Comparison of Multiplication Factors of Fast System Benchmarks Obtained with ENDF/B-VII.0 Data 45

Table A.1 Assumed Temperature and Thermal Expansion Data at Operating Condition 50

Table A.2 Parameters of Fuel Assembly 51

Table A.3 Parameters of Reflector Assembly 52

Table A.4 Parameters of Shield Assembly 52

Table A.5 Parameters of Control Assembly 53

Table A.6 Nuclide Densities of Lower Reflector of Fuel Assembly 57

Table A.7 Nuclide Densities of Active Core Section of Fuel Assembly 57

Table A.8 Nuclide Densities of Gas plenum of Fuel Assembly (Lower Part with Na Bond) 58

Table A.9 Nuclide Densities of Gas plenum of Fuel Assembly (Upper Part) 59

Table A.10 Nuclide Densities of Sodium-Filled Part under Control Rod 59

Table A.11 Nuclide Densities of Control Rod Follower 59

Table A.12 Nuclide Densities of Control Rod 60

Table A.13 Nuclide Densities of Gas Plenum of Control Rod 60
Table A.14 Nuclide Densities of Reflector.....60
Table A.15 Nuclide Densities of Shield 61
Table A.16 Nuclide Densities of Core Barrel and Coolant 61
Table A.17 Nuclide Densities of Lower and Upper Structures 61

List of Figures

Figure 2.1 Core Configuration of 250 MWt ABTR Benchmark Problem 5

Figure 2.2 Comparison of Assembly Power (MWt) Distributions (1/3 core).....21

Figure 3.1 Benchmark Model Geometry for ZPPR-21A (Reference 19) 25

Figure 3.2 Leakage Fraction and Deviation of DIF3D k_{eff} Value from TWODANT Result 31

Figure 3.3 Effects of Separate Spectral Transition Zone between Core and Reflector 32

Figure 3.4 Deviation of TWODANT k_{eff} Value Estimated with Zero Leakage Error from VIM k_{eff} Value vs. Fraction of Main Nuclides in Heavy Metal.....36

Figure A.1 Fuel Assembly Schematics 54

Figure A.2 Control Assembly Schematics 55

Figure A.3 Radial Reflector/Shield Assembly Schematics.....56

Executive Summary

Validation studies of ANL neutronics analysis tools and nuclear data for Advanced Burner Reactor design applications have been initiated. As an initial effort, a numerical benchmark problem based on the reference metal fuel core concept of 250 MWt Advanced Burner Test Reactor (ABTR) and the six ZPPR-21 critical assemblies were analyzed. Preliminary tests of the ENDF/B-VII.0 data were also performed using a set of fast system criticality benchmark problems. Multi-group cross sections were generated using the ETOE-2/MC^2-2 codes based on the ENDF/B-V, ENDF/B-VI, and ENDF/B-VII nuclear data. Deterministic core calculations were performed with the VARIANT nodal transport, TWODANT discrete ordinate transport, and DIF3D diffusion theory codes.

MCNP5 simulations for the ABTR numerical benchmark problem showed a significant dependence of Monte Carlo solutions on the base cross section libraries. The core multiplication factors determined with the ENDF/B-VI and VII data were different by almost 1.0 %Δk. Even different signs were observed among the sodium void worths obtained with different ENDF/B versions, although the sodium void worth of ABTR was estimated to be less than 1$.

Deterministic transport solutions of the ABTR benchmark obtained with 230-group VARIANT calculations showed good agreement with MCNP5 solutions. When all the control assemblies were out of the core, the difference in core multiplication factor was 0.21, -0.1, and 0.22 %Δk for the ENDF/B-V, VI, and VII libraries, respectively. When the control assemblies are fully inserted, this difference increased slightly, but still less than 0.36%. The sodium void worths agreed well with MCNP5 results, generally within 3-sigma Monte Carlo simulation uncertainty. The difference in control assembly worth between VARIANT and MCNP5 solutions was 0.8%, -2.3%, and -1.7% for the ENDF/B-V, VI, and VII libraries, respectively. The isothermal temperature coefficients agreed well with the MCNP5 results within about 2-sigma Monte Carlo simulation uncertainty. The assembly power distributions also agreed with the MCNP5 results within 3-sigma Monte Carlo statistical uncertainty.

When the number of energy groups was reduced from 230 to 33, the core multiplication factor was underestimated by almost 1.0%. However, the prediction accuracy for differential values such as sodium void worth and control assembly worth was deteriorated slightly. The ABTR benchmark problem showed a very large transport effect (~2 %Δk) because of its small core size. The sodium void worth was also significantly underestimated by diffusion theory calculations. However, the control assembly worth and assembly power distribution were predicted very well with diffusion theory.

For all six ZPPR-21 configurations where the Pu-239 concentration varies from 0 to 49 w/o and the U-235 concentration accordingly varies from 62 to 0 w/o, the core multiplication factor determined with 230-group MC^2-2/TWODANT calculation based on the ENDF/B-V.2 data agreed with VIM Monte Carlo solution within 0.20 %Δk and there was no indication of any systematic bias. The quality of principal cross sections generated with the MC^2-2 code was

comparable to that of VIM cross sections. The overall reactivity effect due to the errors in 230-group principal cross sections was estimated to be less than 0.05 %Δk for the ZPPR-21 critical assemblies. The statistics of the differences between calculated values and specified benchmark values showed similar bias and uncertainty for MC^2-2/TWODANT and VIM. This result suggests that the criticality prediction accuracy of MC^2-2/TWODANT is comparable to VIM.

In summary, the ANL suite of deterministic neutronics analysis tools appears to be adequate to use in the initial design stage of Advanced Burner Reactors, of which startup fuel is expected to be conventional plutonium fuel. However, further verification/validation studies need to be performed for transmutation fuel to assess the impact of relatively large amount of minor actinides. In addition, the ETOE-2/MC^2-2 system for multi-group cross section generation needs to be thoroughly tested to process the new ENDF/B-VII data. Several improvements are also highly desirable, including the capability to handle all the ENDF formats for secondary particle energy and angular distributions, proper treatment of fission spectrum dependence on incident neutron energy, and enhanced resonance screening procedures.

1. Introduction

The Advanced Burner Reactor (ABR) based on a fast spectrum is one of the three major technologies to be demonstrated in the Global Nuclear Energy Partnership (GNEP) program. The primary mission of the ABR is to demonstrate the transmutation of transuranics (TRU) recovered from the LWR spent fuel, and hence the benefits of the fuel cycle closure to nuclear waste management. Design of the ABR and confirmation of its safety requires a validated set of analysis tools for representing neutronics, irradiation behavior, thermal-hydraulic, structural and mechanical, and chemical interaction and species transport phenomena in steady-state and transient conditions. Characterization of prediction uncertainties is central to the validation of the analysis tools.

Neutronics validation has been mostly based on the performance of a large number of critical experiments, which allow a global validation of both data and calculation methods of global phenomena. The objective has been to define bias factors and associated uncertainties (to be used to define design/operation margins) for most design integral parameters. The ANL suite of fast reactor neutronics analysis codes has extensively validated against critical experiments [1-5] and high fidelity Monte Carlo solution [6]. The overall neutronics methodologies including depletion calculations have also been validated using a large experimental database derived from destruction measurements of EBR-II experimental test assemblies and processing irradiated EBR-II fuel assemblies in the Fuel Conditioning Facility [7,8].

Compared to conventional fast breeder reactor, however, the ABR would have additional neutronics issues: core and reflector interface effects due to the lack of fertile blanket transition zone, significant transport effects related to enhanced leakage due to a lower fuel density to achieve a lower conversion ratio, and degraded reactivity coefficients due to a higher minor actinide content and a high fissile to fertile ratio. More accurate prediction of fuel evolution is also desirable to characterize the spent fuel with fewer measurements in the reprocessing plant. In addition, The U.S. Cross Section Evaluation Working Group (CSEWG) released in December 2006 the next generation general purpose Evaluated Nuclear Data File, ENDF/B-VII.0 as recommended nuclear data for advanced nuclear science and technology applications [9]. Therefore, validation studies of ANL neutronics analysis tools and nuclear data for ABR design applications have been initiated. As an initial effort, a numerical benchmark problem and a few critical experiments were analyzed.

A numerical benchmark problem was developed based on the reference metal fuel core concept of 250 MWt Advanced Burner Test Reactor (ABTR) [10]. Multi-group cross sections were generated using the ETOE-2/MC^2-2 codes [11,12] based on the ENDF/B-V, ENDF/B-VI, and ENDF/B-VII nuclear data. Core calculations were performed with the VARIANT nodal transport option [13] and DIF3D finite difference and nodal diffusion theory options [14,15]. Core multiplication factor, control assembly worth, sodium void worth, temperature defect, and power distributions were calculated and compared with MCNP5 [16] Monte Carlo solutions. For

MCNP5 Monte Carlo calculations at elevated temperatures, MCNP cross section libraries were generated using the NJOY code [17].

The criticality benchmark problems for the ZPPR-21 critical experiments Phases A through F were analyzed. Multi-group cross sections were generated using the ETOE-2/MC^2-2 codes based on the ENDF/B-V data. Core calculations were performed with the TWODANT discrete ordinate transport code [18]. The predicted multiplication factors were compared with the values provided in the benchmark specifications [19-21] and VIM [22] Monte Carlo solutions.

Preliminary tests of the ENDF/B-VII.0 data were also performed using a set of fast system criticality benchmark problems. Several code modifications were made on the ETOE-2 code. Most of the modifications were associated with the local array dimensions to treat the increased resonance data size. The MC^2-2 code was also modified to treat the fission spectra depending on incident neutron energy. Core multiplications factors were calculated with the TWODANT code and compared with MCNP5 and VIM Monte Carlo solutions.

The ABTR numerical benchmark results are discussed in Section 2, and the analysis results of ZPPR-21 critical experiments are provided in Section 3. Section 4 discusses the preliminary test results of the ENDF/B-VII.0 data. The conclusions are given in Section 5 along with suggestions for future work.

2. Numerical Benchmark Analysis of 250 MWt ABTR

A numerical benchmark problem was developed based on the reference metal fuel core concept of 250 MWt ABTR fueled with weapons grade plutonium. Core multiplication factor, control assembly worth, sodium void worth, temperature defect, and power distributions were calculated and compared with reference Monte Carlo solutions. Cross sections based on the ENDF/B-V, ENDF/B-VI, ENDF/B-VII, and JEF files were used. The analysis methods and results of this ABTR numerical benchmark are discussed in this section.

2.1 Description of ABTR Benchmark Problem

Based on the reference 250 MWt ABTR metal core design fueled with weapons-grade plutonium feed, a numerical benchmark problem was developed with fuel compositions at the beginning of equilibrium cycle. Figure 2.1 shows the core configuration of the benchmark core. The core consists of 194 assemblies: 54 driver, 78 reflector, 48 shield, 10 control, and 9 test assemblies. To facilitate deterministic calculations, the circular core barrel and surrounding sodium were represented by 56 background hexagonal assemblies (Barrel).

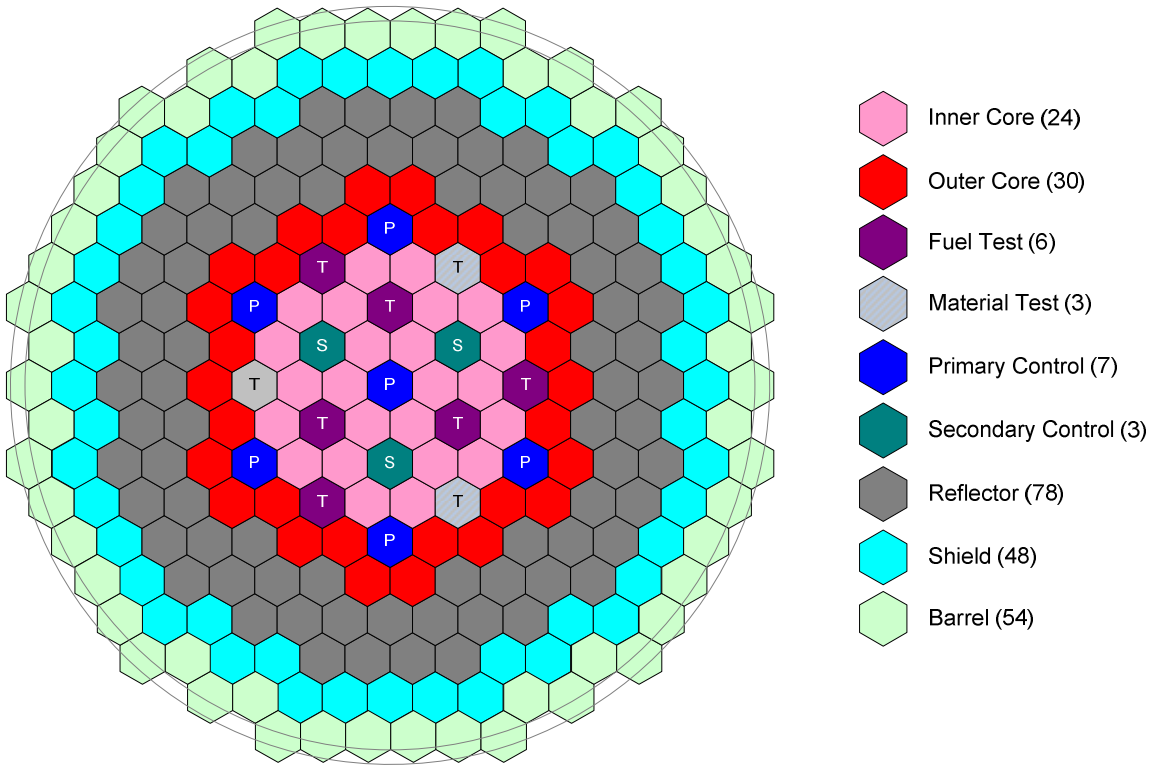

Figure 2.1 Core Configuration of 250 MWt ABTR Benchmark Problem

The core is divided into two enrichments zones: the inner and outer cores composed of 24 and 30 driver assemblies, respectively. Among the nine test assemblies, the six assemblies in the third and fourth rows are fuel test assemblies, and the three assemblies in the fourth row are material test assemblies. The three material test assemblies are assumed to be reflector assemblies. The primary control system consists of one central assembly and six assemblies in the fifth row, and the secondary control system consists of three assemblies in the third row.

The benchmark problem was developed with the fuel compositions at the beginning of equilibrium cycle. Three fuel compositions were derived by averaging the detailed spatial distributions of isotopic number densities determined from an equilibrium cycle analysis over the inner core, outer core, and fuel test assemblies. The geometries and material densities at the assumed operating conditions were used. The material thermal expansion was modeled by adjusting the hexagonal pitch, axial meshes, and fuel and structure material densities appropriately. For simplicity, the wire wrap was smeared with the cladding, and the gap between B_4C pellet and cladding was neglected in the control and shield assemblies. It was also assumed that due to irradiation swelling, the fuel slug is contact with the cladding and the bond sodium is displaced into the lower part of fission gas plenum. To facilitate Monte Carlo simulation, all the fission products were replaced with molybdenum.

Detailed descriptions of assembly geometries and material nuclide densities are provided in Appendix A.

2.2 Cross Section Generation

Using the ETOE-2 code, the MC^2-2 libraries were prepared based on the ENDF/B-V, ENDF/B-VI, and ENDF/B-VII data. In the preparation of MC^2-2 library, wide and extremely weak resonances were pre-processed and represented by the ultra-fine-group (2082 groups) energy structure of MC^2-2. The other resonances were modeled by their resonance parameters, and their self-shielding effects were explicitly evaluated in the MC^2-2 calculation. The resonance data given in the Reich-Moore formalism in the ENDF/B-VI and ENDF/B-VII files were processed with the Adler-Adler representation option, because of a few problems encountered in the more rigorous multi-pole representation option [23]. Most of these problems were resolved later as described in Section 4. For the secondary energy distribution, tabulated function, evaporation spectrum and discrete levels were used. The discrete ultra-fine-group (n,2n) scattering source was approximately treated by neglecting the energy-angle correlation.

For each of the 7 physical zones (inner core, outer core, fuel tests, reflector, shield, lower structure, and upper structure), 33-group and 230-group cross section sets were generated for the specified composition and component-wise temperatures using the MC^2-2 code. Scattering cross sections were prepared up to the P_5 anisotropic scattering order. For each composition, cross sections were generated for three different conditions: base sodium flooded condition at room temperature (for consistent comparison with Monte Carlo solution at room temperature), sodium

voided condition at room temperature, and sodium flooded condition at an elevated temperature (800K).

For the three fuel zones, a critical buckling search calculation was used with a consistent P_1 approximation and the corresponding spectrum was used for group collapsing. For the remaining compositions, a fixed source, derived from the leakage spectrum from an adjacent zone, was used to determine the collapsing spectrum. As an example, the leakage spectrum from the outer core zone was used as a fixed source in the adjoining reflector region to obtain a new collapsing spectrum. The leakage spectrum derived from the reflector calculation was then used as a fixed source in the shield. This process is replicated for all other regions by propagating the leakage from the core through all adjoining regions in the domain.

For resolved resonance integral calculation, the narrow resonance approximation was used, and the Doppler broadening, interference scattering, and the effects of overlap with neighboring resolved resonances were taken into account. An additional option to use the hyper-fine group integral transport calculation with RABANL was also tested, in which the Doppler width is divided into a few hyper-fine groups. The unresolved resonance integral calculation was performed with a narrow resonance approximation, and interference scattering, the effects of overlap with resonances in other spin sequences, and the effects of self-overlap with resonances of the same spin sequences were taken into account. The (n,2n) reaction was treated as a source term in the ultra-fine-group spectrum calculation.

For MCNP5 Monte Carlo calculations, the cross section libraries accompanied with the code were used for the ENDF/B-V and ENDF/B-VI cross sections at room temperature (300K). The ENDF/B-VII cross sections and ENDF/B-V and ENDF/B-VI cross sections at an elevated temperature (800K) were generated using the NJOY code [17]. The ACE format MCNP libraries were generated by a series of runs of NJOY modules for each isotope. The MODER module was first used to convert ENDF tapes to blocked binary modes. With the RECONR module, pointwise cross sections were reconstructed with a tolerance of 0.1%. The BROADR module was then used to perform Doppler-broadening and thinning pointwise cross-sections for a given temperature. The UNRESR and PURR modules were used to compute effective self-shielded pointwise cross sections and probability tables in the unresolved energy range, respectively. The HEATR module was used to generate pointwise heat production cross sections (KERMA factors) as well as radiation-damage-production cross sections. Finally, the ACER model was run to prepare MCNP libraries in ACE format.

2.3 Analysis Methods

The reference solutions of the ABTR numerical benchmark problem were obtained from MCNP5 calculations using three different versions of ENDF data (ENDF/B-V, -VI, and -VII) and JEF-2.2 data. Two different sets of cross sections were tested for each of the ENDF/B-V (*endf5* and *rmccs*) and ENDF/B-VI data (*60c* and *66c*). The "*rmccs*" set accompanied with the MCNP5 code is the recommended ENDF/B-V cross section set by LANL [16]. It is noted that the ENDF/B-V and ENDF/B-VI 60c libraries do not have the probability tables of the unresolved resonance data while they are included in the ENDF/B-VI 66c and ENDF/B-VII.0 libraries. For some nuclides whose cross sections are not provided in the accompanied ENDF/B-V libraries of MCNP5, the ENDF/B-VI libraries were used. Table 2.1 summarizes the isotopic cross sections used in the MCNP5 calculations. The neutron tallies of the MCNP5 calculations were obtained from 5 million neutron histories (100 active cycles with 50,000 neutron histories per cycle) after skipping first 2.5 million histories.

Deterministic calculations were performed with the homogenized assembly models using the DIF3D code. Three flux solution options of DIF3D were examined: finite-difference diffusion theory, nodal diffusion theory, and variational nodal transport theory methods. The nodal option solves the multi-group neutron diffusion equations in two- and three-dimensional hexagonal and Cartesian geometries using the nodal expansion method. Equivalence theory parameters (discontinuity factors) are permitted for hexagonal nodal models. The variational nodal transport theory option (VARIANT) solves the multi-group steady-state neutron transport equation in two- and three-dimensional Cartesian and hexagonal geometries. The nodal equations of the VARIANT option are derived by reformulating the even-parity transport equation as a variational principle and incorporating the odd-parity flux at the interface as a Lagrange multiplier. Anisotropic scattering up to P_5 is treated, and even- and odd-parity fluxes are expanded in orthogonal trial functions of space (up to 50th and 9th order polynomials for even- and odd-parity fluxes, respectively) and angle (spherical harmonics up to P_{15} or simplified spherical harmonics up to 99th order).

For VARIANT transport calculations, the higher order within-group scattering cross sections were modified to be consistent with the total cross section used in VARIANT. In the consistent P_1 or B_1 calculation of MC^2-2 with an extended transport approximation, the multi-group cross sections for each flux moment are weighted with the corresponding flux moment, yielding a consistent set of multi-group equations. On the other hand, the VARIANT code uses total cross sections weighted with a scalar flux as most other transport codes do. That is, the consistent P_N approximation is used. Therefore, the higher order scattering cross sections need to be modified to be consistent with the total cross section weighted with scalar flux as

$$\tilde{\sigma}_{ng'\to g} = \sigma_{ng'\to g} + (\sigma_{t0g} - \sigma_{tng})\delta_{gg'}, \tag{1}$$

Table 2.1 Cross Section Libraries Used in MCNP5 Calculations

Nuclide	ENDF/B-V				ENDF/B-VI				ENDF/B-VII.0	
	endf5 set		rmccs set		ENDF/B-VI-60c		ENDF/B-VI-66c			
	ZAID	ENDF	ZAID	ENDF	ZAID	ENDF	ZAID	ENDF	ZAID [a]	ENDF
U-234	92234.50c	B-V.0	92234.51c	B-V.0	92234.60c	B-VI.0	92234.66c	B-VI.0	92234.00c	B-VII.0
U-235	92235.50c	B-V.0	92235.50c	B-V.0	92235.60c	B-VI.2	92235.66c	B-VI.5	92235.00c	B-VII.0
U-236	92236.50c	B-V.0	92236.51c	B-V.0	92236.60c	B-VI.0	92236.66c	B-VI.0	92236.00c	B-VII.0
U-238	92238.50c	B-V.0	92238.50c	B-V.0	92238.60c	B-VI.2	92238.66c	B-VI.5	92238.00c	B-VII.0
Np-237	93237.50c	B-V.0	93237.60c	B-VI.1	93237.60c	B-VI.1	93237.66c	B-VI.1	93237.00c	B-VII.0
Pu-236	94236.60c	B-VI.0	94236.60c	B-VI.0	94236.60c	B-VI.0	94236.66c	B-VI.4	94236.00c	B-VII.0
Pu-238	94238.50c	B-V.0	94238.51c	B-V.0	94238.60c	B-VI.0	94238.66c	B-VI.0	94238.00c	B-VII.0
Pu-239	94239.50c	B-V.0	94239.55c	B-V.2	94239.60c	B-VI.2	94239.66c	B-VI.5	94239.00c	B-VII.0
Pu-240	94240.50c	B-V.0	94240.50c	B-V.0	94240.60c	B-VI.2	94240.66c	B-VI.2	94240.00c	B-VII.0
Pu-241	94241.50c	B-V.0	94241.51c	B-V.0	94241.60c	B-VI.1	94241.66c	B-VI.3	94241.00c	B-VII.0
Pu-242	94242.50c	B-V.0	94242.51c	B-V.0	94242.60c	B-VI.0	94242.66c	B-VI.0	94242.00c	B-VII.0
Am-241	95241.50c	B-V.0	95241.51c	B-V.0	[c]95241.60c	LANL/T	95241.66c	B-VI.0	95241.00c	B-VII.0
Am-242m	95242.50c	B-V.0	95242.51c	B-V.0	95242.51c	B-V.0	95242.66c	B-VI.1	95242.99c	B-VII.0
Am-243	95243.50c	B-V.0	95243.51c	B-V.0	95243.60c	B-VI.0	95243.66c	B-VI.5	95243.00c	B-VII.0
Cm-242	96242.50c	B-V.0	96242.51c	B-V.0	96242.60c	B-VI.0	96242.66c	B-VI.0	96242.00c	B-VII.0
Cm-243	96243.60c	B-VI.0	96243.60c	B-VI.0	96243.60c	B-VI.0	96243.66c	B-VI.0	96243.00c	B-VII.0
Cm-244	96244.50c	B-V.0	96244.51c	B-V.0	96244.50c	B-VI.0	96244.66c	B-VI.0	96244.00c	B-VII.0
Cm-245	96245.60c	B-VI.2	96245.60c	B-VI.2	96245.60c	B-VI.2	96245.66c	B-VI.2	96245.00c	B-VII.0
Cm-246	96246.60c	B-VI.2	96246.60c	B-VI.2	96246.60c	B-VI.2	96246.66c	B-VI.2	96246.00c	B-VII.0
Zr	[b]40000.56c	B-V:X	40000.60c	B-VI.1	40000.60c	B-VI.1	40000.66c	B-VI.1	40***.00c	B-VII.0
Fe	26000.50c	B-V.0	[c]26000.55c	LANL/T	[d]26***.60c	B-VI.1	26***.66c	B-VI.6	26***.00c	B-VII.0
Ni	28000.50c	B-V.0	28000.50c	B-V.0	28***.60c	B-VI.1	28***.66c	B-VI.6	28***.00c	B-VII.0
Cr	24000.50c	B-V.0	24000.50c	B-V.0	24***.60c	B-VI.1	24***.66c	B-VI.6	24***.00c	B-VII.0
Mn	25055.50c	B-V.0	25055.51c	B-V.0	25055.60c	B-VI.0	25055.66c	B-VI.5	25055.00c	B-VII.0
Mo	42000.50c	B-V.0	42000.51c	B-V.0	42000.60c	B-VI.0	42000.66c	B-VI.0	42100.00c	B-VII.0

[a] Suffix of ENDF/B-VII ZAID was decided arbitrarily by ANL
[b] Modified from "rmccs" library (Appendix G of MCNP4C Users manual).
[c] Cross section was modified by Physics Group T-16 at Los Alamos National Laboratory.
[d] Isotopic cross sections of Fr, Cr, and Ni were used in ENDF/B-VI and –VII cases.

where $\sigma_{ng'\to g}$ is the n-th order scattering cross section from group g' to g, σ_{t0g} is the scalar flux weighted total cross section, σ_{tng} is the total cross section weighted with the n-th flux moment, and $\delta_{gg'}$ is Kronecker's delta.

This correction originates from the multi-group formulation of transport equation. Direct integration of the continuous-energy transport equation over a group interval yields angle-dependent total cross section because of the integral

$$\int_g dE\sigma_t(E)\psi(r,\Omega,E), \tag{2}$$

where σ_t is the total cross section and $\psi(r,\Omega,E)$ is the angular flux. To avoid the angular dependence of the total cross section, the angular flux is expanded into a spherical harmonics series. Then, Eq. (2) is represented as a spherical harmonics series with expansion coefficients containing the total cross sections weighted with flux moments. The formula given in Eq. (1) for anisotropic scattering cross section correction is obtained by moving this series to the right hand side of the neutron balance equation and adding a product of scalar flux weighted total cross section and angular flux to both sides of balance equation [24].

If the energy interval of the integration in Eq. (2) is narrow enough to approximate the energy dependent total cross section as a representative value over the interval, then the total cross section can be taken out of the integral. In this case, the transport correction in Eq. (1) would be zero. This implies that the effect of anisotropic scattering cross section correction would decrease as the number of energy group increases.

2.4 Results

2.4.1 Core Multiplication Factor

Table 2.2 summarizes the core multiplication factors at different core conditions obtained from MCNP5 calculations with different cross section libraries. Three core conditions were considered: base sodium flooded configuration with all control rods out, sodium voided configuration with all control rods (both primary and secondary assemblies) out, and base sodium flooded configuration with all control rods in. In the voided case, all the flowing sodium was removed in the active core and above. In the heterogeneous assembly model, every pin and assembly duct were explicitly modeled, while all materials inside assembly (including duct and inter-assembly gap) were homogenized in the homogenized assembly model. All the MCNP5 calculations were performed at room temperature to utilize the cross sections accompanied with the code.

Table 2.2 Core Multiplication Factors from MCNP5 Calculations [a)]

Coolant			Flooded	Voided	Flooded
Control rods (primary and secondary)			All rods out	All rods out	All rods in
Heterogeneous assembly	ENDF/B-V endf5		1.04223	1.04327	0.92902
	ENDF/B-V rmccs		1.03614	1.03771	0.92486
	ENDF/B-VI 60c		1.04495	1.04444	0.92748
	ENDF/B-VI 66c		1.04738	1.04601	0.92946
	ENDF/B-VII.0		1.03793	1.03744	0.91819
	JEF-2.2		1.04159	1.04190	0.92175
	Difference from endf5 (pcm Δk)	rmccs	-609 ± 34	-556 ± 34	-416 ± 33
		VI-60c	272 ± 36	117 ± 36	-154 ± 33
		VI-66c	515 ± 36	274 ± 33	44 ± 34
		VII.0	-430 ± 34	-583 ± 33	-1083 ± 31
		JEF	-64 ± 35	-137 ± 35	-727 ± 33
Homogenized assembly	ENDF/B-V endf5		1.03922	1.04163	0.91980
	ENDF/B-V rmccs		1.03296	1.03541	0.91577
	ENDF/B-VI 60c		1.04105	1.04115	0.91771
	ENDF/B-VI 66c		1.04328	1.04285	0.91847
	ENDF/B-VII.0		1.03457	1.03429	0.90856
	JEF2.2		1.03882	1.03852	0.91201
	Difference from endf5 (pcm Δk)	rmccs	-626 ± 34	-622 ± 33	-403 ± 30
		VI-60c	183 ± 35	-48 ± 30	-209 ± 29
		VI-66c	406 ± 33	122 ± 36	-133 ± 34
		VII.0	-465 ± 35	-734 ± 33	-1124 ± 29
		JEF	-40 ± 37	-311 ± 33	-779 ± 31

a) Standard deviation of MCNP5 calculations are about ± 0.00025

Tables 2.3 and 2.4 summarize the deterministic calculation results obtained with VARIANT nodal transport and DIF3D nodal diffusion options, respectively. For a consistent comparison with the MCNP5 results, all the cross sections were generated at room temperature. The ENDF/B-V cross sections were generated using the RABANL hyper-fine group transport calculation option. The ENDF/B-VI and ENDF/B-VII cross sections were however generated with the standard narrow resonance approximation, since the effects of hyper-fine group resonance calculation was found small as discussed in Section 2.4.8. For the sodium voided case, unphysical negative cross sections were encountered for some isotopes in the MC^2-2 calculation with the ENDF/B-VII.0 nuclear data. This problem is still under investigation.

Table 2.3 Core Multiplication Factors from Nodal Transport Calculations

Library		Energy groups	Transport option	Flooded, all-rods out	Voided, all-rods out	Flooded, all-rods in
ENDF/B-V		33	[a] P_1P_1 P_3P_1 P_5P_1 P_5P_3	1.01279 1.03020 1.03291 1.03379	1.03502	0.91742
		230	P_5P_1 P_5P_3	1.04130 1.04259	1.04415	0.92085
ENDF/B-VI		33	P_5P_1	1.03334	1.03407	0.91562
		230	P_5P_1	1.04320	1.04456	0.92073
ENDF/B-VII		33	P_5P_1	1.02957	-	0.90869
		230	P_5P_1	1.03678	-	0.91213
Difference from ENDF/B-V	ENDF/B-VI	33	P_5P_1	43	-95	-180
		230	P_5P_1	190	41	-12
	ENDF/B-VII	33	P_5P_1	-334	-	-873
		230	P_5P_1	-452	-	-872

[a] Angular flux approximation order and anisotropic scattering order

Table 2.4 Core Multiplication Factors from Nodal Diffusion Calculations

Library		Energy groups	Flooded, all-rods out	Voided, all-rods out	Flooded, all-rods in
ENDF/B-V		33	1.01516	1.01489	0.90056
		230	1.02256	1.02215	0.90412
ENDF/B-VI		33	1.01488	1.01196	0.89804
		230	1.02389	1.02158	0.90300
ENDF/B-VII		33	1.01211	-	0.89200
		230	1.01822	-	0.89483
Difference from ENDF/B-V	ENDF/B-VI	33	-28	-293	-252
		230	133	-57	-112
	ENDF/B-VII	33	-305	-	-856
		230	-434	-	-930

By comparing the VARIANT nodal transport solutions in Table 2.3 with the MCNP5 solutions for homogenized assembly models in Table 2.2, it can be seen that the VARIANT solutions approach the MCNP5 solutions as the transport solution options are refined by increasing the angular flux and anisotropic approximation orders and the number of energy groups. Table 2.5 compares the VARIANT solutions obtained with P_5 angular flux and P_1 anisotropic scattering approximations with the MCNP5 reference solutions based on the same ENDF/B data. It can be seen that 230-group solutions agree well with the MCNP5 results. For the ENDF/B-V data, the MCNP5 calculations do not use the probability table for unresolved resonance range. It was found that the use of probability tables for unresolved range (i.e., self-shielding of unresolved resonances) increases the multiplication factor by about 200 pcm Δk. Considering this effect, the nodal transport solution agrees with the MCNP5 solution within about 50 pcm Δk. For the cases with all control rods out, the 230-group VARIANT solutions based on the ENDF/B-VI and ENDF/B-VII data agree with the corresponding MCNP5 results within about 200 pcm Δk. For the case with all control rods in, the deviations increase somewhat (up to about 350 pcm Δk). The control rods are closely packed in a duct which slides within the assembly duct. Thus the control rods are confined within a central region with 68% assembly area, but the MC^2-2 calculation was done with homogenized compositions over the entire assembly. The spatial self-shielding effect of boron absorbers could however be treated relatively easily since boron does not have resonances in the energy range of interest.

Table 2.5 Difference in Core Multiplication Factor (pcm Δk) between VARIANT Nodal Transport and MCNP5 Monte Carlo Solutions

Library	Energy groups	Flooded, all-rods out	Voided, all-rods out	Flooded, all-rods in
ENDF/B-V (ENDF/B-V *endf5*)	33	-631	-661	-238
	230	208	252	105
ENDF/B-VI (ENDF/B-VI 66c)	33	-994	-878	-285
	230	-8	171	226
ENDF/B-VII	33	-500	-	13
	230	221	-	357

* P_5 angular flux and P_1 scattering approximations

The transport effect (the difference between transport and diffusion solutions), energy group effect, and anisotropic scattering order effect are summarized in Table 2.6 for the sodium flooded case with all control rods out. The nodal diffusion solutions are about 2% lower than nodal transport solutions, regardless of the number of energy groups and the nuclear data used. This high transport effect is due to the small core size of ABTR. The energy group effect in the deterministic solutions is about 610 to 990 pcm Δk. The transport solutions show about 100 pcm Δk higher group effect than the diffusion solutions. The effect of higher order anisotropic scattering in the nodal transport calculations was evaluated using the ENDF/B-V data. The 230-

group nodal transport solution for P_5 scattering order was not obtained because of limited computer resources; the computation time increases significantly with increasing anisotropic scattering order. Thus, the effect of higher order anisotropic scattering was estimated by comparing the solutions with P_3 and P_1 scattering orders. This effect is about 100 pcm Δk.

Table 2.6 Transport and Neutron Energy Group Effects

Item	Library	Method	Energy groups	Effect (pcm Δk)
Transport effect	ENDF/B-V	Difference between P_5P_1 & diffusion	33	1775
			230	1874
	ENDF/B-VI		33	1846
			230	1931
	ENDF/B-VII		33	1746
			230	1856
Neutron energy group effect	ENDF/B-V	Diffusion	Difference between 230 & 33	740
		Transport		839
	ENDF/B-VI	Diffusion		901
		Transport		986
	ENDF/B-VII	Diffusion		611
		Transport		721
Anisotropic scattering order effect	ENDF/B-V	Difference between P_5P_1 & P_5P_3	33	88
			230	129

* Sodium flooded case with all control rods out.

2.4.2 Nuclear Data Effects

As shown in Table 2.2, the MCNP5 results show a non-negligible variation with the base nuclear data used. Compared to the *endf5* cross section set based on the ENDF/B-V data, the *rmccs* (also based on ENDF/B-V), ENDF/B-VII, and JEF-2.2 cross sections result in consistently lower multiplication factors; the variation is in the range of about -400 to -1100 pcm Δk. In particular, for the case of all rods in, the ENDF/B-VII cross sections yield significantly lower values (by about 1100 pcm) than the other cross section sets. This result indicates that the B-10 cross sections of the ENDF/B-VII data are different from those of other libraries. It is noteworthy that Reference 9 claims that the B-10 cross sections of the ENDF/B-VII data were reevaluated more accurately in collaboration with IAEA and OECD/NEA. Further study needs to done to confirm this claim.

Relative to the *endf5* cross sections, the ENDF/B-VI cross sections (VI-60c and VI-66c) yield generally higher multiplication factors for the cases of all control rods out, but generally lower values for the case of all control rods in. The ENDF/B-VI 66c cross sections result in higher multiplication factor than the ENDF/B-VI 60c cross sections, by about 230 pcm Δk for the sodium

flooded case with all control rods out and by about 160 pcm Δk for the sodium voided case with all control rods out. It is believed that these differences are mainly due to the probability table for unresolved resonance range added to the ENDF/B-VI 66c set. The sodium voided case shows a smaller difference because of its harder spectrum.

It is noted that the *endf5* and *rmccs* sets give different multiplication factors by about 400 to 630 pcm Δk although both of them are based on the same nuclear data, ENDF/B-V, except for a few nuclides. Most noticeable nuclides are Zr and Fe; Zr and Fe in the *rmccs* set are based on the ENDF/B-VI.1 and LANL/T, respectively, as shown in Table 2.1. The effects of these Zr and Fe cross sections were investigated. Additional MCNP5 calculations were performed by substituting Fe and Zr cross sections of the *rmccs* set for those of the *endf5* set. The results shown in Table 2.7 suggest that the significant difference between *endf5* and *rmccs* results is mainly due to the difference in Fe cross sections. When the Fe cross sections were switched from the *endf5* set to the *rmccs* set, the MCNP5 solution decreased by 607 and 631 pcm Δk for the heterogeneous and homogenized assembly models, respectively.

Table 2.7 Core Multiplication Factor Variation by Different Fe and Zr Cross Sections [a)]

Isotopic Library	Assembly model	
	Heterogeneous	Homogenized
All nuclides from ENDF/B-V endf5	1.04223 ± 0.00025	1.03922 ± 0.00026
Fe cross section from *rmccs*	1.03616 ± 0.00024	1.03291 ± 0.00025
Zr cross section from *rmccs*	1.04283 ± 0.00024	1.03899 ± 0.00024
All nuclides from ENDF/B-V *rmccs*	1.03614 ± 0.00023	1.03296 ± 0.00022

a) Flooded sodium case with all control rods out.

As shown in Tables 2.3 and 2.4, the variation of deterministic transport solutions with the base nuclear data shows the same trend as the Monte Carlo solution. Compared to the ENDF/B-V cross sections, the ENDF/B-VII cross sections yield consistently lower multiplication factors by about 330 to 870 pcm Δk. The ENDF/B-VI cross sections results in generally higher values for the cases of all control rods out, but generally lower values for the case of all control rods in. However, the magnitude of variation is somewhat smaller relative to the variation of Monte Carlo solution.

2.4.3 Local Heterogeneity Effects

Local heterogeneity effects were estimated using the MCNP5 solutions obtained with heterogeneous and homogenized assembly models. The total assembly heterogeneity effects determined from the MCNP5 results in Table 2.2 are summarized in Table 2.8. For the base sodium flooded configuration with all control rods out, the heterogeneity effect is about 300 to

400 pcm Δk, depending on the cross section sets used. The mean value of the heterogeneity effects determined with different cross section sets is about 350 pcm Δk, and the standard deviation is about 15%. When the flowing sodium in the active core and above is voided, the local heterogeneity effect generally decreases, with a mean decrease of about 50 pcm Δk, because of spectrum hardening. In the case with all control rods in, the heterogeneity effect increases significantly to about 1000 pcm Δk. The spatial self-shielding effect of control assemblies is much larger than that of fuel assemblies, since the control rods are confined within a central region with 68% assembly area.

Table 2.8 Total Local Heterogeneity Effects (pcm Δk)

	Flooded, all rods out	Voided, all rods out	Flooded, all rods in
ENDF/B-V endf5	301 ± 36	164 ± 31	922 ± 31
ENDF/B-V rmccs	318 ± 32	230 ± 35	909 ± 33
ENDF/B-VI 60c	390 ± 35	329 ± 35	977 ± 31
ENDF/B-VI 66c	410 ± 33	316 ± 37	1099 ± 33
ENDF/B-VII.0	336 ± 34	315 ± 35	963 ± 30
JEF-2.2	277 ± 35	338 ± 36	974 ± 33
Mean [a)]	339 ± 52	282 ± 70	974 ± 67

a) Mean ± one standard deviation.

The heterogeneity effects of pins and duct were separately estimated by homogenizing only the inside of duct. For the fuel assembly, the fuel pins and coolant were homogenized, and the assembly duct and inter-assembly gap were represented explicitly. For the control assembly, only the control rods and coolant within the inner duct were homogenized, and the inner and outer ducts were explicitly modeled. Table 2.9 compares the core multiplication factors obtained from the MCNP5 calculations with the *endf5* cross section set for different fuel assembly models, when all the control assemblies are withdrawn from the active core. As can be seen, the duct heterogeneity effect (249 pcm) is about 5 times larger than the fuel pin heterogeneity effect (52 pcm). This result indicates that most of the fuel assembly heterogeneity effect is due to the duct heterogeneity effect.

The control assembly duct heterogeneity was evaluated by fully inserting all the control assemblies. Table 2.10 compares the core multiplication factors obtained from the MCNP5 calculations with the *endf5* cross section set for different fuel and control assembly models. The duct and pin heterogeneity effects of control assembly are 396 and 26 pcm Δk, respectively. The heterogeneity effect of control assembly is about one and half times larger than that of fuel assembly.

Table 2.9 Pin and Duct Heterogeneity Effects of Fuel Assembly (pcm Δk)

Fuel and control assembly models	k-effective or Δk

1	Heterogeneous assembly	1.04223 ± 0.00025
2	Homogenized pins (homogenized inside of duct)	1.04171 ± 0.00023
3	Homogenized assembly (homogenized pins & duct)	1.03922 ± 0.00025
- Duct heterogeneity effect (case 2 – case 3) - Pin heterogeneity effect (case 1 – case 2) - Pin and duct heterogeneity effect (case 1 – case 3)		249 ± 34 52 ± 34 301 ± 36

Table 2.10 Pin and Duct Heterogeneity Effects of Control Assembly (pcm Δk)

Assembly model (fuel/control)		k-effective or Δk
1	Heterogeneous assembly / Heterogeneous assembly	0.92902 ± 0.00024
2	Heterogeneous / Homogenized pins (homogenized inside)	0.92876 ± 0.00019
3	Heterogeneous assembly / Homogenized assembly	0.92480 ± 0.00023
- Control assembly duct heterogeneity effect (case 2 – case 3) - Control pin heterogeneity effect (case 1 – case 2) - Control pin and duct heterogeneity effect (case 1 – case 3)		396 ± 30 26 ± 31 422 ± 33

2.4.4 Sodium Void Worth

The sodium void worth was evaluated in dollar ($) unit using the core multiplication factors summarized in Tables 2.2, 2.3, and 2.4, using a delayed neutron fraction of 330 pcm Δρ [10]. The calculated sodium void worth is provided in Table 2.11. Depending on the cross section sets used, the sodium void worth determined from the MCNP5 calculations varies from -0.4$ to 0.4$ for the heterogeneous assembly model and from -0.1$ to 0.7$ for the homogenized assembly model. For both the heterogeneous and homogenized assembly models, the ENDF/B-V data yield a positive sodium void worth but the ENDF/B-VI 66c and ENDF/B-VII.0 data result in a negative worth. The sodium void worth calculated with the ENDF/B-VI 60c and JEF-2.2 data is very small and changes its sign between the heterogeneous and homogenized assembly models. It is noted that the sodium void worth of this ABTR benchmark problem is very small because of its small core size and most MCNP5 results are less than 3-sigma Monte Carlo simulation uncertainty. In general, the homogenized assembly model has higher sodium void worth by about 0.3$ than the heterogeneous assembly model.

The sodium void worth values calculated with VARIANT solutions with homogenized assembly models agree well with those of MCNP5 results, generally within 3-sigma Monte Carlo simulation uncertainty. Compared to the transport solution, however, the diffusion theory solution consistently underestimates the sodium void worth because of overestimated neutron leakage.

Table 2.11 Sodium Void Worth ($)

Assembly model	Nuclear Data	MCNP5	Nodal transport (33/230 group)	Nodal diffusion (33/230 group)
Heterogeneous assembly	ENDF/B-V endf5	0.29 ± 0.1	Not available in deterministic calculations	
	ENDF/B-V rmccs	0.44 ± 0.1		
	ENDF/B-VI 60c	-0.14 ± 0.1		
	ENDF/B-VI 66c	-0.38 ± 0.1		
	ENDF/B-VII.0	-0.14 ± 0.1		
	JEF-2.2	0.09 ± 0.1		
Homogenized assembly	ENDF/B-V endf5	0.67 ± 0.1	0.64 / 0.87	-0.31 / -0.12
	ENDF/B-V rmccs	0.69 ± 0.1		
	ENDF/B-VI 60c	0.03 ± 0.1	0.22 / 0.41	-0.88 / -0.79
	ENDF/B-VI 66c	-0.12 ± 0.1		
	ENDF/B-VII.0	-0.08 ± 0.1	-	-
	JEF2.2	-0.08 ± 0.1	-	-

2.4.5 Control Assembly Worth

Tables 2.12 and 2.13 summarize the reactivity worth of control assemblies determined from MCNP5 Monte Carlo and deterministic calculations, respectively. The MCNP5 results show some variations, depending on the cross section sets used. The reactivity worth of all the assemblies in both primary and secondary systems varies from 35.4$ to 38.1$ for the heterogeneous assembly model, and from 37.5$ to 40.6$ for the homogenized assembly model. The ENDF/B-VII.0 data results in about 1.4$ higher control rod worth than the ENDF/B-VI (66c) data, which in turn yields another 1.3$ higher worth than the ENDF/B-V (endf5) data. As discussed in Section 2.2.4, the B-10 cross sections of the ENDF/B-VII appear to be different from those of other libraries because they are revaluated recently. The mean value is 36.7$ for the heterogeneous assembly model and 39.2$ for the homogenized assembly model. The homogenized assembly model gives about 2.5$ larger total control assembly worth than the heterogeneous assembly model. The standard deviation is about 3% for both models.

The reactivity worth of the primary system varies from 20.9$ to 22.6$ for the heterogeneous assembly model, and from 22.2$ to 24.1$ for the homogenized assembly model. The mean value is 21.9$ for the heterogeneous assembly model and 23.1$ for the homogenized assembly model. The standard deviation is about 3% for both models. As in the total control assembly worth, the reactivity worth of the primary system increases with evolving ENDF/B versions. The reactivity worth of the secondary system is 14.6$ for the heterogeneous assembly model and 15.5$ for the homogenized assembly model. The reactivity worth per assembly of the secondary system (~4$) is larger than that of the primary system (~3$) because the secondary control assemblies are in higher neutron importance region. The central control assembly has the largest worth (~6$).

Table 2.12 Control Assembly Worth from MCNP5 Calculations ($)

		All assemblies	Primary assembly	Secondary assemblies	Central assembly
Number of control assemblies		10	7	3	1
Heterogeneous assembly	ENDF/B-V endf5	35.4 ± 0.1	21.1 ± 0.1	14.6 ± 0.1	5.9 ± 0.1
	ENDF/B-V rmccs	35.2 ± 0.1	20.9 ± 0.1	-	-
	ENDF/B-VI 60c	36.7 ± 0.1	21.8 ± 0.1	-	-
	ENDF/B-VI 66c	36.7 ± 0.1	22.2 ± 0.1	-	-
	ENDF/B-VII.0	38.1 ± 0.1	22.6 ± 0.1	-	-
	JEF-2.2	37.8 ± 0.1	22.6 ± 0.1	-	-
	Mean	36.7 ± 1.2	21.9 ± 0.7	-	-
Homogenized assembly	ENDF/B-V endf5	37.8 ± 0.1	22.4 ± 0.1	15.5 ± 0.1	6.5 ± 0.1
	ENDF/B-V rmccs	37.5 ± 0.1	22.2 ± 0.1	-	-
	ENDF/B-VI 60c	39.1 ± 0.1	23.0 ± 0.1	-	-
	ENDF/B-VI 66c	39.5 ± 0.1	23.2 ± 0.1	-	-
	ENDF/B-VII.0	40.6 ± 0.1	24.0 ± 0.1	-	-
	JEF2.2	40.6 ± 0.1	24.1 ± 0.1	-	-
	Mean [a)]	39.2 ± 1.3	23.1 ± 0.8	-	-

a) Mean ± one standard deviation.

Table 2.13 Control Assembly Worth from Deterministic Calculations ($)

Library		ENDF/B-V		ENDF/B-VI		ENDF/B-VII	
Energy groups		33	230	33	230	33	230
Nodal transport (P_5P_1 solution)	All	36.9	38.1	37.7	38.6	39.2	39.9
	Primary	21.6	22.3	22.1	22.8	23.0	23.7
	Secondary	15.6	15.8	15.9	16.1	-	-
	Central	6.4	6.4	6.5	6.9	-	-
Nodal diffusion	All	38.0	38.8	39.6	40.6	40.3	41.0
	Primary	21.9	22.5	22.4	23.1	23.4	24.0
	Secondary	15.9	16.2	16.3	16.6	-	-
	Central	6.1	6.0	6.2	6.3	-	-

The control assembly worth determined from deterministic calculation shows a similar trend to the MCNP5 results; the control assembly worth increases with evolving ENDF/B versions. The control assembly worths determined from deterministic transport and diffusion theory calculations agree well with the MCNP5 result. The differences between 230-group VARIANT and MCNP5 results for the total control assembly worth are 0.8%, -2.3%, and -1.7% for the ENDF/B-V (endf5), ENDF/B-VI (66c), and ENDF/B-VII data, respectively. The reactivity worths of primary system, secondary system, and central assembly are also predicted by the 230-group VARIANT solutions within 2.0% deviation from the MCNP5 results. The 33-group VARIANT results show somewhat larger deviations up to 4.7%. The 230-group diffusion theory

results also agree with the MCNP5 results with a maximum deviation of 4.5%. The 33-group diffusion theory results are within 6.2% deviation from the MCNP5 results.

2.4.6 Isothermal Temperature Coefficients

Using the homogenized assembly model, the isothermal temperature coefficients were estimated by increasing the temperature uniformly from 300K to 800K over the whole core. To eliminate the potential inconsistency between the libraries generated at 800K and the libraries for 300K accompanied with the MCNP5 code, the libraries at 300K were also regenerated. The estimated temperature coefficients are summarized in Table 2.14, including the effects of the probability table for unresolved resonance range. Compared to the ENDF/B-VI.8 and ENDF/B-VII.0 data, the ENDF/B-V.2 data yield noticeably smaller temperature coefficients. This discrepancy is attributed to the different releases of Fe cross sections as discussed in Section 2.4.2. The core multiplication factor decreases by about 420 to 580 pcm when the temperature is uniformly increased from 300K to 800K, resulting temperature coefficients of -1.19 to -1.61 ¢/K. The effect of the probability table for unresolved resonance range is about 200 pcm at 300K, but it becomes negligible at 800K because Doppler broadening reduces the self-shielding effect. It is noted that the temperature coefficients obtained in this benchmark calculations are about an order of magnitude higher than the Doppler effect of the reference 250 MWt ABTR design (~0.1 ¢/K) because the temperature effect was evaluated at lower temperature (from 300K to 800K) compared to the temperature used in the reference ABTR design (from 850K to 1700K).

The isothermal temperature coefficients determined from 230-group VARIANT calculations agree well with the MCNP5 results within about 2-sigma Monte Carlo simulation uncertainty. The 33-group VARIANT results and the nodal diffusion theory results yield similarly larger deviations from the MCNP5 results.

Table 2.14 Isothermal Temperature Coefficient (¢/K)

Library	Use of Probability Table	MCNP5	Nodal transport (33/230 group) [a)]	Nodal diffusion (33/230 group)
ENDF/B-V.2	No	-0.76 ± 0.12	-	-
	Yes	-1.19 ± 0.12	-1.31 / -1.26	-1.35 / -1.30
ENDF/B-VI.8	No	-1.14 ± 0.12	-	-
	Yes	-1.61 ± 0.12	- 1.06 / -1.35	-1.09 / -1.15
ENDF/B-VII.0	Yes	-1.56 ± 0.12	-	-

[a)] 33 and 230 group deterministic calculations

2.4.7 Assembly Power Distribution

The assembly power distributions were also calculated using the homogenized assembly model. Figure 2.2 shows the assembly power distributions in MWt. The reference solution was

obtained from the MCNP5 calculations with the ENDF/B-V (endf5) library using the energy deposition tally F6. The average standard deviation of the fuel assembly powers in the MCNP5 solution is about ±0.021 MWt. Three different deterministic solutions obtained with 230-group flux calculations are compared with the MCNP5 power distribution: nodal diffusion solution with ENDF/B-V cross sections, and nodal transport (VARIANT) solutions with ENDF/B-V and ENDF/B-VI cross sections. Generally, the assembly power distributions of the deterministic calculations agree with the reference solution within 3-sigma Monte Carlo statistical uncertainty, regardless of solution methods and nuclear data.

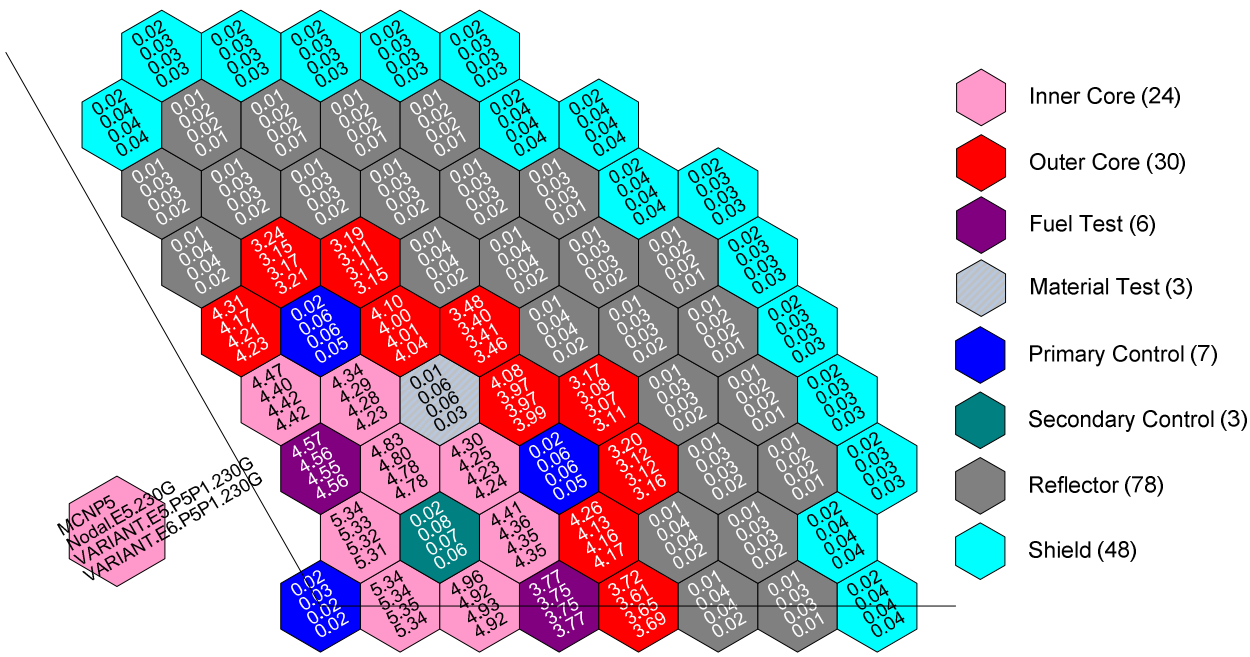

Figure 2.2 Comparison of Assembly Power (MWt) Distributions (1/3 core)

2.4.8 Effects of Anisotropic Scattering Correction and Refined Resonance Absorption

As discussed in Section 2.3, the higher order within-group scattering cross sections generated from MC^2-2 calculations need to be modified to be consistent with the total cross section weighted with scalar flux used in the VARIANT code. The effect of this within-group scattering cross section correction was examined. As shown in Table 2.15, the effect of within-group scattering cross section correction is more than 3% in 33-group structure. This result confirms that the within-group scattering cross sections of all the anisotropic scattering orders should be consistent with the total cross section used in the transport calculation.

For resolved resonance integral calculation, the MC^2-2 code uses the narrow resonance approximation. An alternative RABANL option to use the hyper-fine group integral transport

calculation is also available. The RABANL option provides a rigorous treatment of resolved resonance cross sections and is intended for use in the lower energy ranges for which the narrow resonance approximation is not valid. The RABANL module performs a hyper-fine-group slowing down calculation by dividing the resolved resonance Doppler width into a few groups. The effect of the RABANL option was evaluated by comparing the core multiplication factors obtained with 33-group cross section sets generated with narrow resonance approximation and the RABANL option. The refined resonance absorption effect turned out to be only about 60 pcm Δk. The results indicate that the narrow resonance approximation is adequate for the ABTR benchmark problem because of its hard spectrum.

Table 2.15 Effects of Within-group Scattering Cross Section Correction and Hyper-Fine-Group Resonance Calculation

Item	Library	Method	Groups	Effect (pcm Δk)
Within-group scattering XS correction	ENDF/B-V	Transport	33	3056
Hyper-fine-group resonance calculation	ENDF/B-V	Diffusion	33	63
		Transport	33	61

3. Analysis of ZPPR-21 Critical Experiment Benchmarks

The criticality benchmark problems for the ZPPR-21 critical experiments Phases A through F were analyzed. Multi-group cross sections were generated using the ETOE-2/MC^2-2 codes based on the ENDF/B-V.2 data. Core calculations were performed with the TWODANT discrete ordinate transport code. The predicted multiplication factors were compared with the values provided in the benchmark specifications in References 19 to 21 and VIM Monte Carlo solutions. The analysis methods and results of these ZPPR critical benchmark problems are discussed in this section.

3.1 Description of ZPPR-21 Critical Experiments

The ZPPR Assembly 21 consists of a series of six criticality benchmark cores built in the ZPPR facility to provide data for validating criticality calculations for systems likely to arise in the Integral Fast Reactor (IFR) fuel processing operations. The assemblies are graphite reflected, and different mixtures of plutonium and uranium are used in mock-up Pu/U/zirconium fuel. The first of these configurations, ZPPR-21A, was built with only plutonium fuel to take advantage of the inherent neutron source of Pu-240. Then enriched uranium was progressively substituted for plutonium in Phases 21B through 21E. The final configuration, ZPPR-21F, has an all-uranium fuel loading and required an external neutron source to assist in the approach to critical. Experiments in Assembly 21 were performed between June and September 1990.

All six configurations have the same core volume which approximates a cylinder of about 40 cm height and a stepped radial boundary of about 19 cm effective radius. Mass loadings of the principal core constituents in the six ZPPR 21 reference configurations reported in Reference 19 are given in Table 3.1. Note that the zirconium content remained constant through all the phases, while the U-238 and steel varied by only small amounts.

Table 3.1 Principal Mass Loadings in the ZPPR-21 Cores (kg) [a)]

Material	21A	21B	21C	21D	21E	21F
Pu-239	94.4	74.9	55.4	35.9	16.4	0.0
Pu-240	5.9	4.9	4.0	3.1	2.2	0.0
Pu-241	0.20	0.18	0.16	0.14	0.12	0.00
U-235	0.2	20.5	61.1	81.4	122.0	162.6
U-238	90.4	91.6	94.0	95.2	97.6	98.3
Zr	30.7	30.7	30.7	30.7	30.7	30.7
Steel [b)]	74.7	80.5	78.8	84.2	82.0	79.5

[a)] Minor quantities of C, O, Al, Si, P, Cl, S, Cu, Mo, U-234, U-236, Pu-238, and Am-241 are not shown.

[b)] Steel includes Fe, Ni, Cr, and Mn.

The reactivity of the reference critical configuration for each of the ZPPR-21 phases was obtained from an inverse kinetics analysis of the power history when the fuel control rods were fully inserted and the B_4C shim rods were fully withdrawn. Reference configuration data for the six mixed-fissile phases are given in Table 3.2. The benchmark models were developed based on the VIM analyses for the as-built models in References 19 to 21, where all the experimental details were represented. The key features retained in the benchmark models are the region-averaged compositions, region volumes, and the global RZ geometry. The radial dimensions of the benchmark model are determined by the total cross-sectional area of the matrix positions included in each region, i.e., radii of cylindrical boundaries conserve cross-sectional areas of the corresponding regions in the detailed model. Axial dimensions of each region conserve the region volume. Masses of the constituents within these regions are then homogenized to produce the region-averaged compositions, thereby conserving material masses within each region. The VIM output edits for the as-built model included the region-average compositions, which were extracted to construct the benchmark model.

Table 3.2 Reference Configuration Data for ZPPR-21

Configuration	21A	21B	21C	21D	21E	21F
Loading No.	18	30	34	49	57	66
Date	07/11/1990	07/24/1990	08/01/1990	08/10/1990	08/21/1990	09/04/1990
Temperature, °C	26	26	25	24	23	22
Experimental k_{eff}	1.00023	1.00009	0.99928	1.00135	1.00092	1.00056
Adjusted Experimental k_{eff}	1.00085 ±0.00150	1.00071 ±0.00144	0.99980 ±0.00148	1.00179 ±0.00152	1.00124 ±0.00166	1.00057 ±0.00177
Benchmark Model k_{eff}	0.9967 ±0.0026	0.9897 ±0.0023	0.9998 ±0.0023	1.0018 ±0.0024	1.0012 ±0.0024	0.9998 ±0.0025

References 19 to 21 illustrate the reduction procedures in detail to develop the proposed benchmark problems in a concise, easy-to-reproduce RZ geometry benchmark model and to derive the core eigenvalue for each benchmark problem. The experimental k_{eff} in Table 3.2 was adjusted to account for the effects of matrix interface gap, matrix tube pitch gap, room return neutron, impurities (including corrosion impurities), and Ke-F coating material for the depleted-uranium plate, which are not included in the benchmark specifications. The adjusted experimental k_{eff} was further corrected by the reactivity effects corresponding to the geometry transformation from the as-built model to the RZ geometry benchmark model, yielding the benchmark model k_{eff} value that is included in the last row of Table 3.2 along with the one standard deviation. The benchmark eigenvalues account for cylinderization effect, heterogeneity effect (plate, drawer, and matrix tube), and homogenization effect of each region. Even with this significant simplification, transport effect, energy group effect, energy self-shielding and material interference, modeling concerns, and basic cross section effect can be addressed with the benchmark model.

The benchmark model geometry for ZPPR-21 Phase A is depicted in Figure 3.1. Except the thicknesses of the radial reflector and voided drawers, all the benchmark geometries remain the same throughout all the phases of ZPPR-21. The radial reflector thickness is 8.05415 cm for 21A, 12.59858 cm for 21B, 9.95114 cm for 21C, 16.06981 cm for 21D, 12.79081 cm for 21E, and 8.77122 cm for 21F.

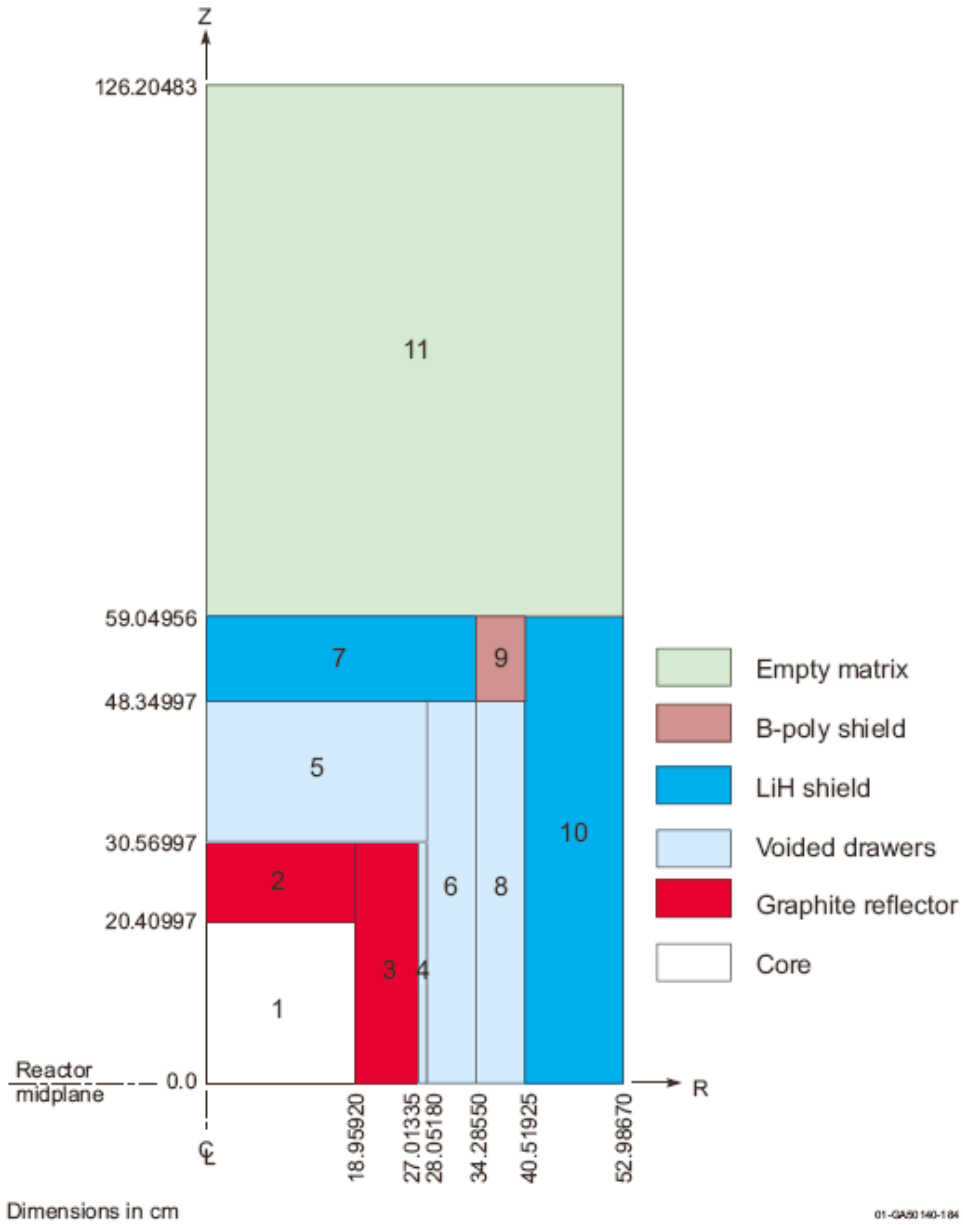

Figure 3.1 Benchmark Model Geometry for ZPPR-21A (Reference 19)

3.2 Cross Section Generation

For each configuration, region-dependent 230-group cross sections were generated using the MC^2-2 code based on the ENDF/B-V.2 data. MC^2-2 calculations were performed with the consistent P_1 approximation, and anisotropic scattering cross sections were generated for Legendre orders up to five. The critical buckling search was performed for the active core region.

For non-fueled regions, fixed source calculations were performed with an estimated leakage spectrum from adjacent region. For example, the MC^2-2 calculations for regions 2 and 3 in Figure 3.1 were performed with an external source representing the leakage spectrum of region 1. Two paths of neutron leakage were assumed; one sequence of 1, 2, 5, 7, and 11 and the other sequence of 1, 3, 4, 6, 8, and 10.

Since there were significant amount of steel in critical assemblies, it was necessary to shield resonance-like Fe scattering cross section in the energy above the resolved resonance energy region. Using the SHIELD program [25], the smooth cross section library of MC^2-2 was generated for each specific composition and used in the subsequent region-wise MC^2-2 calculation.

The resulting cross section set for each region was augmented for all the regions of an assembly using the SDX code. The fundamental flux weighted total cross section is used as the total cross section in the TWODANT calculations. Accordingly, the higher order within-group scattering cross sections were modified to be consistent with the flux weighted total cross section.

3.3 Reference VIM Monte Carlo Calculations

Reference solutions were obtained from VIM Monte Carlo calculations with the cross sections based on the ENDF/B-V.2 data. Thirty million histories were used per each assembly. The k_{eff} values are summarized in Table 3.3. The cited VIM k_{eff} values were obtained from the combined estimator of analog and track length estimators. The standard deviation was rounded up from the fifth decimal point. For all the six core configurations, the standard deviation of Monte Carlo simulation is less than or equal to 20 pcm Δk. With such a small standard deviation, the isotopic reaction rate edited from the VIM calculations can be used for a detail comparison with the TWODANT results.

Table 3.3 k_{eff} Results for ZPPR-21 Phases A through F from VIM Calculations

Configuration	A	B	C	D	E	F
Benchmark k_{eff}	0.9967 ±0.0026	0.9897 ±0.0023	0.9998 ±0.0023	1.0018 ±0.0024	1.0012 ±0.0024	0.9998 ±0.0025
VIM k_{eff} (ENDF/B-V.2)	1.0000 ±0.0002	0.9925 ±0.0002	0.9979 ±0.0002	0.9997 ±0.0002	1.0000 ±0.0002	1.0005 ±0.0002
Deviation, pcm Δk	330	280	-190	-210	-120	70

The VIM k_{eff} results for the configurations C to F agree with the benchmark k_{eff} values within one standard deviation of benchmark k_{eff}. The results for the configurations A and B show slightly larger deviations from the benchmark values; the deviations are between one and two standard deviations of benchmark k_{eff}.

3.4 TWODANT Core Calculation

Fine mesh RZ geometry models were developed for TWODANT calculations with 1 cm radial and axial mesh intervals to eliminate the mesh related errors. For example, the TWODANT model for ZPPR-21A has 52 radial meshes and 122 axial meshes. Using these fine mesh models, sensitivity studies were first performed for anisotropic scattering order and angular quadrature. Then, the effects of anisotropic scattering correction and core-reflector interference were investigated.

3.4.1 Effect of Scattering Order and Angular Quadrature

Table 3.4 compares the TWODANT k_{eff} results for different orders of anisotropic scattering approximation. All the results were obtained with a S_N order of 24 (i.e., 78 different angles per octant) and triangular Chebyshev-Legendre built-in constants. The fifth and sixth columns list the k_{eff} differences from the P_1 calculation results.

Table 3.4 TWODANT (S_{24}) k_{eff} Values of ZPPR-21 Cores vs. Anisotropic Scattering Order

Scattering order	P_1	P_3	P_5	P_3-P_1 (pcm)	P_5-P_1 (pcm)
A	0.99192	0.99860	0.99873	668	681
B	0.98747	0.99285	0.99293	538	546
C	0.99131	0.99690	0.99698	559	567
D	0.99596	1.00036	1.00042	440	446
E	0.99545	1.00002	1.00008	457	463
F	0.99331	0.99843	0.99852	512	521

It is noted that the P_1 approximation significantly underestimates core k_{eff} values. This implies that the diffusion calculations with the transport corrected diffusion coefficients are expected to significantly underestimate core k_{eff} values for these configurations. Expansion up to the third Legendre order of anisotropic scattering yields almost converged core k_{eff} values, within 13 pcm of more refined P_5 calculation results. There is no essential difference between P_3 and P_5 scattering expansion results. These results suggest that at least P_3 approximation needs to be used for ZPPR-21 analyses. This is a characteristic of such small cores like ZPPR-21 assemblies.

Table 3.5 presents the dependency of TWODANT k_{eff} values on angular quadrature. The triangular Chebyshev-Legendre built-in constants were used for S_{24} and S_{32}, while the traditional

built-in constants were used for S_{16}. The value in each parenthesis designates the k_{eff} difference from the S_{16} result for each Legendre scattering order. As can be seen, the k_{eff} value almost converges to an asymptotic value when the quadrature order is greater than or equal to 24. Based on this result, S_{24} was selected for angular quadrature.

Table 3.5 TWODANT k_{eff} Values of ZPPR-21 Cores vs. Angular Quadrature Order

Scattering order	P_3			P_5	
Angular quadrature	S_{16}	S_{24}	S_{32}	S_{16}	S_{24}
A	0.99899	0.99860 (-39)[a)]	0.99855 (-44)	0.99912	0.99873 (-39)
B	0.99317	0.99285 (-32)	0.99281 (-36)	0.99321	0.99293 (-28)
C	0.99724	0.99690 (-34)	0.99685 (-39)	0.99732	0.99698 (-34)
D	1.00062	1.00036 (-26)	1.00033 (-29)	1.00067	1.00042 (-25)
E	1.00030	1.00002 (-28)	0.99998 (-32)	1.00035	1.00008 (-27)
F	0.99876	0.99843 (-33)	0.99839 (-37)	0.99885	0.99852 (-33)

[a)] Deviation from S_{16} results in pcm Δk.

3.4.2 Effect of Anisotropic Scattering Cross Section Correction

The effect of the anisotropic within-group scattering cross section correction was examined. Table 3.6 summarizes the correction effect determined from 230-group P_5S_{24} TWODANT calculations. As can be seen, the effect of anisotropic scattering correction is noticeable even in 230-group structure; the correction effect is -218 pcm Δk on average. Since the fundamental flux weighted total cross section is used as a total cross section in TWODANT, the corrected cases correspond to the consistent P_5 approximation. Compared to the VIM Monte Carlo solutions, the TWODANT results without correction of anisotropic within-group scattering cross sections overestimate the core k_{eff} by 170 pcm Δk on the average, while the results with the correction underestimate the core k_{eff} by 50 pcm Δk on the average.

Table 3.6 TWODANT (P_5S_{24}) k_{eff} Values of ZPPR-21 Cores vs. Anisotropic Within-Group Scattering Cross Section Correction

Configuration	VIM	No Correction	Correction	Difference (pcm)
A	1.0000±0.0002	1.00127	0.99873	-254
B	0.9925±0.0002	0.99506	0.99293	-213
C	0.9979±0.0002	0.99931	0.99698	-233
D	0.9997±0.0002	1.00225	1.00042	-183
E	1.0000±0.0002	1.00199	1.00008	-191
F	1.0005±0.0002	1.00084	0.99852	-232
VIM-TWODANT [a)]		-0.0017±0.0009	0.0005±0.0011	

a) Mean ± one standard deviation.

3.4.3 Transport Effect

Table 3.7 compares the TWODANT results and DIF3D finite difference diffusion theory results. Both codes used the same cross section set and the same mesh arrangement. Thus, the large difference between two solutions can be attributed to the transport effect. In such a small core like ZPPR-21 where transport effect is large, the diffusion theory approximation should be applied with caution. Comparing the results in Table 3.7 with the TWODANT solutions with P_1 scattering order in Table 3.4, it can be seen that linearly anisotropic scattering comprises only 7% of the total transport effect. The remaining 93% of the transport effect comes from the neutron streaming effect which is not considered in the diffusion theory.

Table 3.7 Comparison of k_{eff} Values of ZPPR-21 Cores Obtained from TWODANT Transport and DIF3D Diffusion Theory Calculations

Configuration	TWODANT P_5	DIF3D FDM	Difference (% Δk)
A	0.99873	0.90010	-9.863
B	0.99293	0.91406	-7.887
C	0.99698	0.91395	-8.303
D	1.00042	0.93424	-6.618
E	1.00008	0.93066	-6.942
F	0.99852	0.92054	-7.798

The main difference between transport and diffusion theory calculations is the difference in neutron leakage treatment, and thus the leakage effects were examined in detail. Table 3.8 compares the leakage fractions among total effective neutron losses of TWODANT and DIF3D solutions. The reactivity effects of the differences in leakage and main reactions between DIF3D and TWODANT solutions are also provided. Both TWODANT and DIF3D solutions were normalized to the same production rate. As expected, the DIF3D diffusion theory solutions overestimate the neutron leakage by about 3 to 4%. The overestimated leakage leads to underestimation of core reactivity by about 7 to 11 %Δρ. The reactivity effects of the differences in fission, capture, and (n,2n) reactions are insignificant. These results suggest that the difference in the core flux distribution between TWODANT and DIF3D solutions is not significant.

To examine the leakage estimation by the diffusion theory further, a parametric study was performed by increasing the active core size of ZPPR-21A arbitrarily in a radial direction with a fixed core height of 1 m. Table 3.9 summarizes the leakage fractions and the reactivity effects of the differences in leakage and main reactions between DIF3D diffusion theory and TWODANT P_1S_{16} solutions. As can be seen, the difference in the leakage fraction between TWODANT and DIF3D solutions decreases with increasing core size, and the reactivity error of DIF3D diffusion theory solution decreases noticeably with decreasing leakage fraction. The leakage fraction and deviation of DIF3D k_{eff} value from TWODANT solution are also shown in Figure 3.2 as a function of surface to volume ratio of the active core. The leakage fraction is approximately

proportional to the surface to volume ratio, and thus the surface to volume ratio can serve as a rough indicator to resort to the transport theory solution for a given core size. The results in Figure 3.2 suggest that a core with a surface to volume ratio greater than 0.047 or a leakage fraction larger than 0.18 would generally demand the use of transport theory solution in order to keep the deviation of diffusion theory k_{eff} value from transport solution to remain less than 0.5 %Δρ.

Table 3.8 Comparison of Leakage Fraction and Main Reaction Rates between TWODANT Transport and DIF3D Diffusion Theory Solutions for ZPPR-21 Cores

Configuration		A	B	C	D	E	F
Leakage Fraction	TWODANT	0.5958	0.5702	0.5561	0.5251	0.5156	0.5128
	DIF3D	0.6367	0.6044	0.5936	0.5557	0.5491	0.5512
	Difference	0.0409	0.0342	0.0375	0.0306	0.0335	0.0384
Reactivity Effect [a)] (%Δρ)	Leakage	-11.08	-8.70	-9.17	-6.99	-7.44	-8.52
	Fission	0.00	-0.01	0.00	-0.02	-0.01	0.00
	Capture	0.11	0.02	0.06	-0.06	0.00	0.04
	(n,2n)	0.00	-0.01	-0.01	-0.01	-0.01	-0.01

a) Reactivity effect of the deviation of DIF3D solution from TWODANT solution.

Table 3.9 Comparison of Leakage Fraction and Main Reaction Rates between TWODANT P_1S_{16} and DIF3D Diffusion Theory Solutions vs. Core Size (ZPPR-21A Compositions)

Core Radius (cm)		18.9592	50	75	100	125	150
Core Height (cm)		40.8199	100	100	100	100	100
Leakage Fraction	TWODANT	0.5961	0.2565	0.1825	0.1468	0.1270	0.1151
	DIF3D	0.6367	0.2698	0.1906	0.1526	0.1318	0.1192
	Difference	0.0407	0.0133	0.0081	0.0059	0.0048	0.0041
Reactivity Effect [a)] (%Δρ)	Leakage	-11.02	-0.96	-0.48	-0.32	-0.25	-0.21
	Absorption	0.11	0.09	0.06	0.05	0.04	0.04
	(n,2n)	-0.00	-0.10	-0.08	-0.07	-0.07	-0.06

a) Reactivity effect of the deviation of DIF3D solution from TWODANT solution.

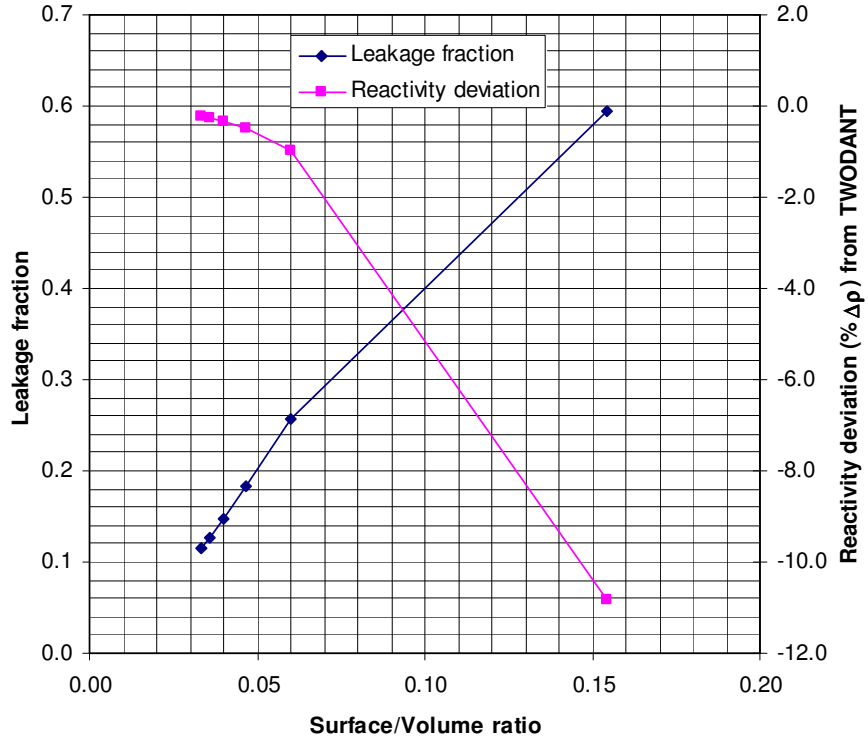

Figure 3.2 Leakage Fraction and Deviation of DIF3D k_{eff} Value from TWODANT Result

3.4.4 Core-Reflector Interface Effect

Because of the graphite reflector in the ZPPR-21 Assemblies, the spectrum of the neutrons reflected into the core would be softer than that of the neutrons leaking into the reflector. Thus, U-238 would have enhanced probability to capture neutrons in the core of ZPPR-21 assemblies than in an infinite medium of the same core compositions. In addition, since graphite does not have overlapping resonances with U-238, the background cross section for U-238 resonance absorption would be enhanced if core-reflector interface is modeled in more detail.

In order to account for these effects together, the core was divided into two regions, and a separate set of cross sections was generated for the region adjacent to the reflector using a mixture of core and reflector materials. Based on the observation that the average ratio of incoming to outgoing partial currents at the core-reflector interface of ZPPR-21 assemblies is 0.56, the mixture was made of ~64% core material and ~36% of reflector material. Two separate TWODANT calculations were performed using the mixture cross sections for the core region within one and two absorption mean free paths from the reflector.

The results are shown in Figure 3.3 as a function of Pu-239 fraction (w/o) in heavy metal. In case of using the mixture cross section within one mean free path, the correction amounts to 18 pcm for ZPPR-21F and 47 pcm for ZPPR-21B. The absorption mean free path is 2.14 cm for

ZPPR-21F and 2.54 cm for ZPPR-21B. Even when the region for the mixture cross sections was increased to two mean free paths, the results are almost identical. On the average, the core-reflector interference effect is -34 pcm for SMEAR-1 and -39 pcm for SMEAR-2. These small effects are considered due to the hard neutron spectrum of the ZPPR-21 cores which makes the resonance absorption less important.

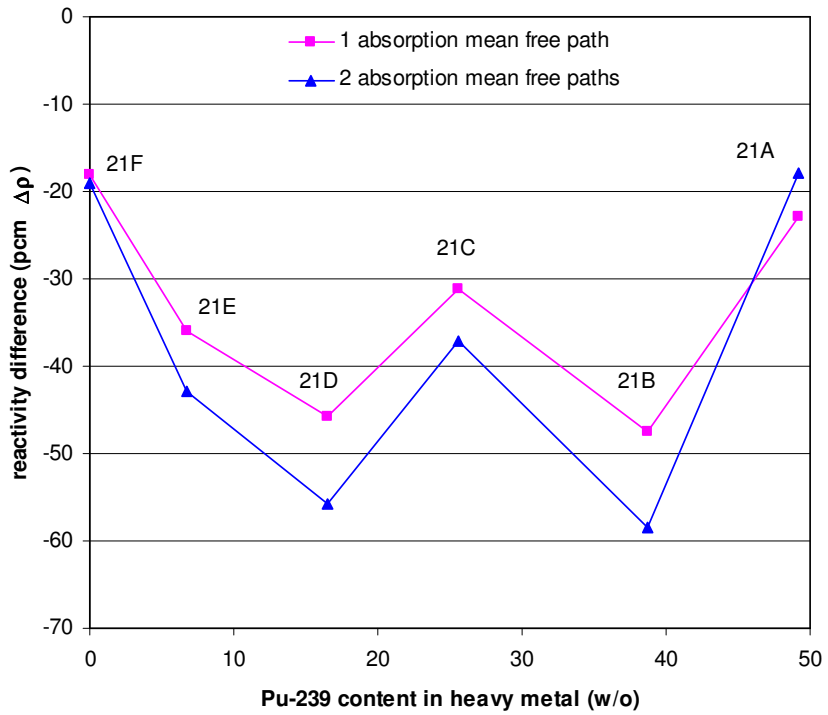

Figure 3.3 Effects of Separate Spectral Transition Zone between Core and Reflector

3.5 Verification of MC^2-2/TWODANT against VIM Monte Carlo Calculation

Based on the modeling studies discussed in the previous section, TWODANT P_5S_{24} transport calculation results obtained with 230-group cross sections generated with MC^2-2 are considered to be the best estimates practically achievable with deterministic codes. These TWODANT results are compared in detail with the VIM Monte Carlo solutions. Isotopic contributions to the deviation between TWODANT and VIM core reactivity values were investigated. From 230-group P_5S_{24} TWODANT calculations, isotopic one-group cross sections were extracted together with leakage rate. Isotopic one-group macroscopic cross sections determined with the track length estimator were also extracted from VIM calculations. Tables 3.10 and 3.11 summarize the reactivity effects caused by the deviations of TWODANT one-group cross sections from VIM results. Only the isotopes that contribute more than 1 pcm are listed. The scattering is presented by the difference in macroscopic cross sections between TWODANT and VIM solutions, while the other reactions are given in terms of reactivity effects.

Table 3.10 Reactivity Effects (pcm) of Deviations of TWODANT One-Group Cross Sections from VIM Results (ZPPR-21 Phase A through C)

Nuclide	21A					21B					21C				
	nu	n,2n	cap	fiss	scat*	nu	n,2n	cap	fiss	scat*	nu	n,2n	cap	fiss	scat*
P-239	-12	-1	63	-87	-1	-11	0	74	-96	1	-1	0	52	-85	-1
P-240	-1	0	42	-1	0	-1	0	56	-3	0	0	0	32	0	0
P-241	0	0	0	1	0	0	0	0	0	0	0	0	0	-1	0
P-242	0	0	-1	0	0	0	0	-1	0	0	0	0	0	0	0
Am-241	0	0	-2	0	0	0	0	-2	0	0	0	0	0	0	0
U-234						0	0	-1	0	0	0	0	0	0	0
U-235	0	0	0	0	0	-3	0	4	-1	0	-2	1	12	-30	-1
U-236						0	0	0	0	0	0	0	0	0	0
U-238	-4	-3	61	-18	0	-3	-3	68	-19	3	-3	2	52	-11	-2
Cr	0	0	0	0	-4	0	0	0	0	-2	0	0	1	0	-3
Ni	0	0	2	0	-1	0	0	2	0	0	0	0	1	0	-1
Fe	0	0	-9	0	-5	0	0	-12	0	-3	0	0	-8	0	-4
Mo	0	0	2	0	0	0	0	2	0	0	0	0	1	0	0
Mm-55	0	0	0	0	0	0	0	-1	0	1	0	0	0	0	0
Zr	0	0	-8	0	6	0	0	-9	0	9	0	0	-6	0	6
Sum over nuclides, pcm	-17	-5	150	-105	-5	-18	-4	180	-120	10	-6	3	136	-127	-6
Leakage, pcm	-176					-15					-92				
δk/k (estimated), pcm	-153					24					-88				
δk/k (calculated), pcm	-153					24					-94				
δk/k (estimated w/o leakage error), pcm	23					39					2				
Reflector thickness (cm)	8.1					12.6					10.0				

* $(\Sigma_{s,TWODANT}-\Sigma_{s,VIM}) \times 10^5$ [cm^{-1}]

Table 3.11 Reactivity Effects (pcm) of Deviations of TWODANT One-Group Cross Sections from VIM Results (ZPPR-21 Phase D through F)

Nuclide	21D					21E					21F				
	nu	n,2n	cap	fiss	scat*	nu	n,2n	cap	fiss	scat*	nu	n,2n	cap	fiss	scat*
P-239	4	0	64	-146	1	3	0	31	-67	0					
P-240	0	0	47	-2	0	0	0	21	0	0					
P-241	1	0	0	-1	0	0	0	0	-1	0					
P-242	0	0	-1	0	0	0	0	0	0	0					
Am-241	0	0	0	0	0	0	0	1	0	0					
U-234	0	0	1	0	0	0	0	2	0	0	0	0	2	0	0
U-235	-6	0	4	17	2	-3	-1	20	-57	0	7	0	38	-131	-3
U-236	0	0	1	0	0	0	0	2	0	0	0	0	1	0	0
U-238	-1	-1	72	-12	2	-1	-1	54	-7	-1	0	0	40	-1	-4
Cr	0	0	0	0	-2	0	0	1	0	-2	0	0	0	0	-2
Ni	0	0	1	0	1	0	0	1	0	0	0	0	0	0	-1
Fe	0	0	-13	0	-2	0	0	-8	0	-3	0	0	-5	0	-1
Mo	0	0	1	0	0	0	0	1	0	0	0	0	0	0	0
Mm-55	0	0	-1	0	1	0	0	0	0	1	0	0	0	0	0
Zr	0	0	-8	0	8	0	0	-5	0	6	0	0	-3	0	4
Sum over nuclides, pcm	-3	-2	170	-145	11	-1	-2	118	-132	1	7	-1	75	-131	-8
Leakage, pcm	37					25					-140				
δk/k (estimated), pcm	57					8					-190				
δk/k (calculated), pcm	56					8					-191				
δk/k (estimated w/o leakage error), pcm	19					-17					-51				
Reflector thickness (cm)	16.1					12.8					8.8				

* $(\Sigma_{s,TWODANT}-\Sigma_{s,VIM}) \times 10^5$ [cm^{-1}]

In Tables 3.10 and 3.11, "δk/k (estimated)" is the deviation of TWODANT reactivity value from VIM result estimated with the isotopic reaction rates, and "δk/k (calculated)" is the deviation determined with the k_{eff} values of TWODANT and VIM calculations. These two values agree each other. The difference is 7 pcm for the ZPPR-21C configuration and is less than 1 pcm for the other cases. This result indicates that the neutron balance edits of TWODANT are consistent with the cross section edits. This implies that the cross sections generated with MC^2-2 and subsequently corrected for within-group anisotropic scattering cross sections are well balanced. Since TWODANT indirectly determines the removal cross sections from the total and within-group scattering cross sections, any inconsistency between total and partial cross sections or improper treatment of (n,2n) cross section would cause a non-negligible difference between k_{eff} values determined with isotopic cross sections and reaction balance.

The TWODANT reactivity values differ from VIM results by -153, 24, -94, 56, 8, and -191 pcm Δρ for ZPPR-21A through 21F, respectively. The correlation coefficients between reactivity deviations and heavy metal contents are estimated to 0.00 for Pu-239, -0.06 for U-235, and 0.32 for U-238. That is, there is no noticeable correlation between reactivity deviation and heavy metal content. However, there is a strong correlation between reactivity deviation and reflector thickness. The TWODANT underestimates the k_{eff} value for the configurations 21A, 21C, and 21F whose reflector is thinner than 10.0 cm, but overestimates for the configurations 21B, 21D, and 21E whose reflector is thicker than 12 cm. The correlation coefficient between reactivity deviation and reflector thickness is 0.94. This result suggests that reflector cross sections or scattering cross sections of core material need to be improved for enhanced accuracy. However, this reflector effect would diminish in a power reactor where the active core radius is much larger than the ZPPR-21 cores, because of reduced surface to volume ratio. In addition, a graphite reflector used in the ZPPR-21 cores is not likely to be used in power reactor.

The effects of isotopic cross section differences were examined by isolating the leakage effects. By using the leakage fractions determined from VIM calculations in the neutron balances of TWODANT calculations, the leakage errors of TWODANT calculations were arbitrarily eliminated. An additional reactivity deviation was estimated and included as "δk/k (estimated w/o leakage error)" in Tables 3.10 and 3.11. The estimated reactivity values without leakage error are off from the reference VIM values by 23, 39, 2, 19, -17, and -51 pcm Δρ for ZPPR-21A through 21F, respectively. These deviations are plotted in Figure 3.4 as a function of main isotope fractions in heavy metal. The estimated k_{eff} value with zero leakage error shows an increasing trend with increasing Pu-239 content, but a decreasing trend with increasing U-235 content. The magnitude of variation is however small, within ±50 pcm, for a wide range of Pu-239 or U-235 fraction. In addition, in a mixture of Pu-239 and U-235, they tend to cancel the error each other. The situation is somewhat different for U-238. Although the range of U-238 fraction is rather narrow (from 37.3 to 47.5 w/o), U-238 shows almost perfect correlation with the reactivity deviation; the correlation coefficient between reactivity deviation and U-238 fraction is about 0.99. If this trend is extrapolated to a U-238 content of 80 w/o (as in typical

power reactor) by neglecting the interaction effects among different nuclides, it is expected that MC^2-2/TWODANT would overestimate the core k_{eff} value by 290 pcm relative to VIM.

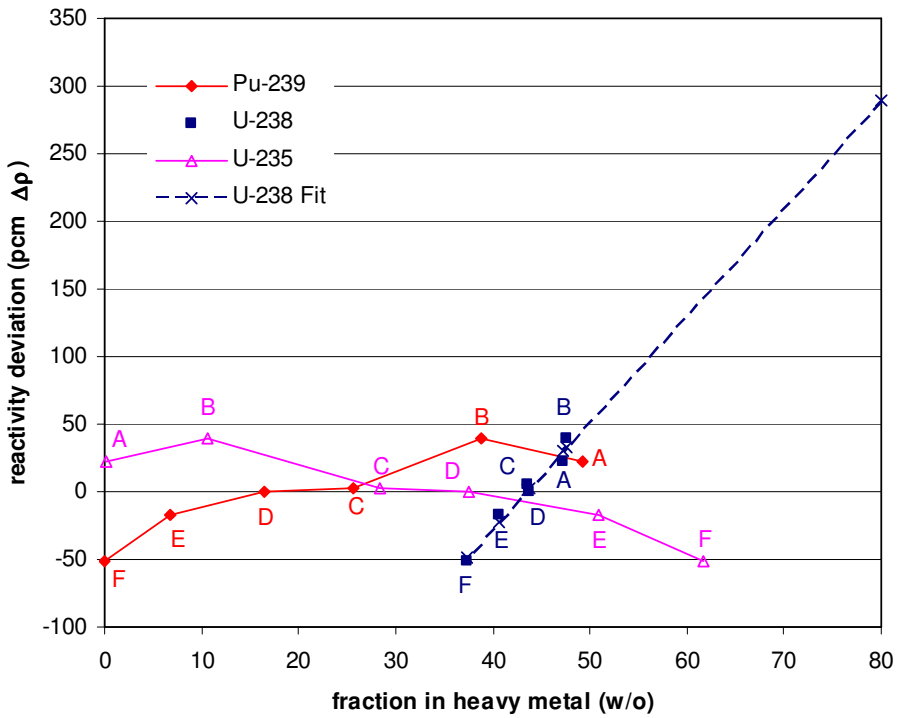

Figure 3.4 Deviation of TWODANT k_{eff} Value Estimated with Zero Leakage Error from VIM k_{eff} Value vs. Fraction of Main Nuclides in Heavy Metal

The isotopic reaction results in Tables 3.10 and 3.11 show that the deterministic calculation with MC^2-2/TWODANT underestimates both fission and capture reactions of most of actinides relative to VIM. The underestimated capture and fission reactions respectively make positive and negative contributions to the reactivity. In the ZPPR-21 cores, the total contribution of capture reactions is in the range of 75 to 180 pcm, and the total contribution of fission reactions is in the range of -105 to -142 pcm. These positive and negative contributions are cancelled each other, yielding a net contribution in the range of about -50 to 50 pcm.

In the ZPPR-21A core where Pu-239 is the main fissile isotope, Pu-239 contribution is -36 pcm, and the contribution of all the Pu isotopes is almost zero. The 23 pcm deviation from VIM value mainly comes from the U-238 contribution. In the ZPPR-21B, Pu-239 content is reduced relative to ZPPR-21A, thus Pu-239 contribution is reduced slightly to -34 pcm. The total contribution of all the Pu isotopes increases to 18 pcm, most of which is due to reduced capture reactions. The total contribution of U-238 is 43 pcm, and this is the main contributor to the positive reactivity deviation from VIM, as in ZPPR-21A. In the case of ZPPR-21F where U-235 is the only fissile nuclide, the negative reactivity deviation from VIM is mainly due to the

underestimated U-235 fission. The results in Tables 3.10 and 3.11 also indicate that the resonance absorption of Pu-240 and U-238 are underestimated by MC^2-2/TWODANT relative to VIM.

In this study, resonance-like Fe cross sections above the resonance region were self-shielded using the SHIELD program. The difference in Fe scattering cross sections between TWODANT and VIM shown in Tables 3.10 and 3.11 indicate that Fe cross sections were properly self-shielded. The effects of this Fe cross section shielding were estimated to be 63, 73, 71, 70, 74, and 65 pcm for ZPPR-21A through 21F, respectively.

3.6 Validation of MC^2-2/TWODANT against Benchmark Experimental Values

Table 3.12 compares the TWODANT core k_{eff} results with benchmark values. For comparison purposes, VIM results are also included. TWODANT results were obtained from P_5S_{24} calculations with shielded Fe cross sections. The TWODANT k_{eff} values are well within 1-sigma measurement uncertainty, except for ZPPR-21B and 21C. For ZPPR-21B and 21C, the deviation is between 1 and 2-sigma uncertainties. The mean and 1-sigma standard deviation of the differences between TWODANT and benchmark k_{eff} values for six configurations are -20 and 230 pcm, respectively. As can be seen, TWODANT results are very consistent with VIM results. The correlation coefficients between reactivity deviations and heavy metal contents indicate that Pu-239 and U-238 contribute to overestimation of the core k_{eff} and U-235 contributes to underestimation.

Table 3.12 Comparison of TWODANT k_{eff} Results with Benchmark Values

	Benchmark	VIM	TWODANT	VIM-Benchmark, pcm Δk	TWODANT-Benchmark, pcm Δk
21A	0.9967±0.0026	1.0000±0.0002	0.99873	330	200
21B	0.9897±0.0023	0.9925±0.0002	0.99293	280	320
21C	0.9998±0.0023	0.9979±0.0002	0.99698	-190	-280
21D	1.0018±0.0024	0.9997±0.0002	1.00042	-210	-140
21E	1.0012±0.0024	1.0000±0.0002	1.00008	-120	-110
21F	0.9998±0.0025	1.0005±0.0002	0.99852	70	-130
Mean ± one standard deviation of (C-M), pcm Δk				30 ± 240	-20 ± 230
Correlation coefficient with Pu-239				0.78	0.70
Correlation coefficient with U-238				0.60	0.68
Correlation coefficient with U-235				-0.75	-0.70

Along with the verification results against VIM calculations discussed in Section 3.5, these results for the ZPPR-21 critical assemblies show that (1) the accuracy of the MC^2-2/TWODANT system for core k_{eff} estimation is comparable to the VIM Monte Carlo code, and (2) the multi-

group cross sections generated with MC^2-2 are accurate to reproduce the isotopic reaction rates of VIM calculations with a good accuracy.

3.7 Group Collapsing Methods

Although the 230-group MC^2-2/TWODANT calculations produce accurate solutions comparable to VIM Monte Carlo results, the computational time is typically too long to be practical for routine design calculations. As an attempt to devise a more efficient procedure for routine design calculation, therefore, several methods to collapse fine-group cross sections to broad-group cross sections were examined.

Direct generation of broad-group cross sections from MC^2-2 calculations was first tested. For each composition in the core, 33-group cross sections were generated directly from MC^2-2 calculations. Then, TWODANT calculations were performed using these 33-group cross sections. The resulting core k_{eff} values are compared with 230-group solutions in Table 3.13. These values deviate from the 230-group solutions by -423, -309, -353, -250, -264, and -376 pcm, respectively, for the ZPPR-21 configurations A through F. Examination of reaction rates indicated that most of these deviations were due to the differences in the leakage rates, but in the case of ZPPR-21D, about 25% of the deviation was attributed to the differences in production and absorption rates. These results suggest a need to use a group collapsing scheme as a standard method of generating broad-group cross sections.

Table 3.13 k_{eff} Results of ZPPR-21 Cores Obtained with Different Group Collapsing Methods

Configuration	A	B	C	D	E	F
230 Group, Consistent P_5	0.99873	0.99293	0.99698	1.00042	1.00008	0.99852
33 Group, Consistent P_5	0.99453	0.98989	0.99348	0.99793	0.99745	0.99479
230G $\Rightarrow$ 33G, ϕ_0 -weighted, Consistent P_5	1.00085	0.99530	0.99914	1.00274	1.00224	1.00047
230G $\Rightarrow$ 33G, $\lvert\phi_{n,0}\rvert$-weighted, Consistent P_5	0.99896	0.99303	0.99708	1.00036	1.00005	0.99859
230G $\Rightarrow$ 33G, $\sum_m \lvert\phi_{m,n}\rvert$ -weighted, Consistent P_5	0.99901	0.99326	0.99721	1.00068	1.00025	0.99864

Scalar flux weighting was tested at first. All the 230-group cross sections were collapsed to region-wise 33-group cross sections using the scalar flux obtained from 230-group TWODANT calculations, and then TWODANT calculations were repeated with these 33-group cross sections.

The resulting core k_{eff} values are included in Table 3.10 as "230G $\Rightarrow$ 33G, ϕ_0 -weighted." Compared to the reference 230-group solutions, the resulting 33-group solutions overestimate the core k_{eff} value by 212, 237, 216, 231, 215, and 195 pcm for the ZPPR-21 configurations A through F, respectively. It was found that most of these deviations were attributed to the reduced leakage out of the core region. In other words, the current out of the core was not preserved between 230-group and 33-group TWODANT calculations. This is due to the total flux weighting used for collapsing higher order scattering cross sections.

In multi-group transport theory calculations, the scattering source of order n from a group g' to a group g in the direction Ω is represented as

$$\sum_{m=-n}^{n} \Sigma_{g'\to g}^{n} \phi_{n,m}^{g'} Y_{n,m}(\Omega)\,, \tag{3}$$

where $\Sigma_{g'\to g}^{n}$ is the n-th order scattering cross section, $\phi_{n,m}^{g'}$ is the spherical harmonics moment of the angular flux of group g', and $Y_{n,m}(\Omega)$ is the spherical harmonic function evaluated at direction Ω. To preserve the scattering source of order n from a broad-group G' to a broad-group G, the broad-group scattering cross section from G' to G needs to be defined as

$$\Sigma_{G'\to G}^{n} \sum_{m=-n}^{n} \phi_{n,m}^{G'} Y_{n,m}(\Omega) = \sum_{g\in G} \sum_{g'\in G'} \Sigma_{g'\to g}^{n} \sum_{m=-n}^{n} \phi_{n,m}^{g'} Y_{n,m}(\Omega)\,. \tag{4}$$

Since the spherical harmonics are orthogonal to each other, this equation represents $2n+1$ independent equations

$$\Sigma_{G'\to G}^{n} \phi_{n,m}^{G'} = \sum_{g\in G} \sum_{g'\in G'} \Sigma_{g'\to g}^{n} \phi_{n,m}^{g'}, \quad -n \le m \le n\,. \tag{5}$$

Thus higher order scattering cross sections cannot be defined uniquely to preserve the scattering source for all directions.

For collapsing higher order scattering cross sections, two weighting spectra were tested. The first one was the spectrum of $\phi_{n,0}$ as used in the cross section generation codes based on one-dimensional unit cell transport calculations. This is equivalent to selecting a direction and preserving the higher order scattering sources in this direction. However, the angular flux moments calculated from a fine-group transport calculation cannot be used directly as a weighting spectrum. The higher flux moments for a fixed direction may change their sign within a broad group at low energy. For example, at a core and reflector interface, the fine-group higher order moments are positive (i.e., directed toward the reflector) for the higher energy part of the broad group and negative (i.e., directed toward the core) for the lower energy part of the broad group. As a result, the summation of the fine-group flux moments in this broad group become very small or even negative, yielding unphysical broad-group scattering cross sections. Under the assumption that the flux moments are separable in energy and space within each broad group and a spatial region over which the group collapsing is to be done, the sign change of flux moments can be attributed to the spatial part and then the energy part becomes positive. Therefore, the

absolute value of $\phi_{n,0}$ was used as the weighting spectrum. The TWODANT calculation results obtained using the region-dependent 33-group cross sections collapsed with $|\phi_{n,0}|$ are included in Table 3.10 as "230G $\Rightarrow$ 33G, $|\phi_{n,0}|$-weighted." As can be seen, the 33-group calculations almost reproduce the 230-group results; the deviations are only 23, 10, 10, -6, -3, and -7 pcm for ZPPR-21 A through F, respectively.

The second approach was to use the summation of the flux moments corresponding to each scattering order; that is, $\Sigma_{m=-n}^{n} |\phi_{n,m}|$ was used as the weighting spectrum. The TWODANT calculation results obtained using the region-dependent 33-group cross sections collapsed with this approach are included in Table 3.10 as "230G $\Rightarrow$ 33G, $\sum_m |\phi_{m,n}|$-weighted." The results are essentially the same to those obtained with the $|\phi_{n,0}|$ spectrum. These results suggest that either $|\phi_{n,0}|$ or $\Sigma_{m=-n}^{n} |\phi_{n,m}|$ can be used for collapsing higher-order scattering cross sections.

4. Preliminary Tests of ENDF/B-VII Data

As discussed in Section 2, the ENDF/B-VII.0 data was processed and used for the ABTR numerical benchmark analysis. Additional preliminary tests of the ENDF/B-VII.0 data were performed using a set of fast system criticality benchmark problems. Multi-group cross sections were generated using the ETOE-2 and MC^2-2 codes. Core multiplications factors were calculated with the TWODANT code and compared with MCNP5 and VIM Monte Carlo solutions.

Using the ENDF/B-VII.0 data, the MC^2-2 libraries were prepared with the ETOE-2 code. Using the RIGEL code, ENDF files for each isotope were converted to binary files for use in ETOE-2. Because of significantly increased data in the ENDF/B-VII.0 data for some isotopes such as U-238, Th-232, Zr-90, etc., the ETOE-2 code was modified to treat the changes made in the ENDF/B-VII data; for instance, the number of resonances of U-238 was increased from 1653 in ENDF/B-VI to 3343 in ENDF/B-VII.0. Most of the problems were resolved by increasing the size of data arrays in the ETOE-2 code. However, there are still outstanding issues as discussed below. If necessary, alternative options were used to circumvent these issues.

Since the MC^2-2 code allows only three laws for inelastic and (n,2n) scattering among the six energy distribution laws for secondary particles available in the ENDF/B format, the data provided in the other three laws were converted into tabulated functions with the ETOE-2 code. Similar alternations were applied in the processing of fission spectrum and angular distributions of elastic scattering. The Reich-Moore parameters for resolved resonances were converted to multi-pole parameters that preserve the general features required by the traditional resonance integral concept and the Doppler-broadening algorithm in the MC^2-2 code without comprising rigor. In addition, two types of resonances were screened out into composition and temperature independent ultra-fine group smooth cross sections: (1) very wide resonances with natural widths (Γ_n) much larger than both the corresponding Doppler width (Γ_d) and the ultra-fine group width (i.e., $\Gamma_n / \Gamma_d > 50$) and (2) very weak or narrow resonances belonging to the medium weight nuclei of low natural abundance or p-wave resonances of heavy nuclei, which have small Doppler effect and self-shielding effect contributions. Detailed criteria on screening of wide and weak resonances are discussed in Reference 26.

In the ENDF/B-VII.0 data, the energy distribution of fission neutrons is given as a function of incident neutron energy for more fissionable isotopes compared to the previous ENDF/B-V and ENDF/B-VI data. The fission spectra of U-234, U-238, Pu-241, and Th-232 depend on the incident neutron energy in ENDF/B-VII.0; the fission spectrum dependent on the incident neutron energy was provided for Pu-239 from ENDF/B-V and for U-235 from ENDF/B-VI. However, the ETOE-2 code constructs the fission spectrum of each fissionable isotope using an effective incident neutron energy specified by the user. For example, the values of 3 MeV, 500 keV, and 300 keV were conventionally used for U-238, Pu-239, and U-235, respectively.

Important isotopes pertinent to sodium-cooled fast reactors were successfully processed into the MC^2-2 library formats. Table 4.1 summarizes the resolved and unresolved resonance data in

Table 4.1 Resonance Data (ENDF/B-VII.0) of Isotopes Used in the ABTR Benchmark

Isotope	Resolved				Unresolved	Isotope	Resolved				Unresolved
	Type*	Original Number	Screened Number	Upper Energy Boundary (keV)	Upper Energy Boundary (keV)		Type*	Original Number	Screened Number	Upper Energy Boundary (keV)	Upper Energy Boundary (keV)
Na-23	MB	23	9	500	-	Mo-96	MB	75	62	19	100
Cr-50	RM	386	321	792	-	Mo-97	MB	66	55	2	100
Cr-52	RM	223	183	980	-	Mo-98	MB	158	109	32	100
Cr-53	RM	131	118	200	-	Mo-100	MB	124	99	26	100
Cr-54	RM	116	146	900	-	Th-232	RM	927	465	4	100
Fe-54	RM	380	384	700	-	U-233	RM	770	735	0.6	40
Fe-56	RM	311	280	850	-	U-234	MB	119	118	1.5	100
Fe-57	RM	75	83	200	-	U-235	RM	3193	3163	2.25	25
Fe-58	RM	68	85	400	-	U-236	RM	117	116	1.5	100
Mn-55	MB	149	89	100	-	U-238	RM	3343	3312	20	149
Ni-58	RM	482	415	812	-	Np-237	MB	760	545	0.5	35
Ni-60	RM	272	256	450	-	Pu-238	SB	16	14	0.2	10
Ni-61	RM	32	17	70	-	Pu-239	RM	1070	691	2.5	30
Ni-62	RM	57	38	600	-	Pu-240	MB	268	263	5.7	40
Ni-64	RM	52	31	600	-	Pu-241	RM	244	210	0.3	40.2
Ga-69	MB	27	15	4.5	-	Pu-242	SB	68	67	0.986	10
Ga-71	MB	30	16	5.6	-	Am-241	SB	195	196	0.15	30
Zr-90	MB	89	17	60	400	Am-242m	MB	106	98	0.043	27.2832
Zr-91	MB	95	80	20	100	Am-243	SB	220	216	0.25	42.3751
Zr-92	MB	101	60	71	100	Cm-242	SB	13	12	0.276	10
Zr-94	MB	73	52	90	100	Cm-243	SB	105	103	0.1	42.1743
Zr-96	MB	30	13	100	-	Cm-244	MB	68	67	1	40
Mo-92	MB	77	64	50	100	Cm-245	MB	91	78	0.1	54.9553
Mo-94	MB	55	46	20	100	Cm-246	MB	17	17	0.4	43.0277
Mo-95	MB	56	46	2.1412	206.2685	-	-	-	-	-	-

* SB: Single-level Breit-Wigner, MB: Multi-level Breit-Wigner, AA: Adler-Adler, RM: Reich-Moore.

ENDF/B VII.0 of the isotopes that have been processed by the ETOE-2 code. Wide and weak resonances were screened out by the rules mentioned above. The resonance data given in the Reich-Moore formalism were converted into the multi-pole representation. However, the resonance data of Pu-239 and Th-232 could not be processed correctly with the multi-pole representation option, and hence they were temporarily processed with the Adler-Adler representation option.

Preliminary analyses for the Los Alamos fast critical assemblies showed that neglecting the dependence of fission spectrum on incident neutron energy introduced about 100 to 400 pcm difference in criticality prediction. Using the NJOY code with its fast spectrum weighting function option, therefore, the fission spectra of major isotopes, U-238, U-235, and Pu-239, were generated in the ultra-fine (2082) group structure of MC^2-2. The MC^2-2 code was modified to use these fission spectra in its ultra-fine group spectrum calculation.

For verification of the MC^2-2 libraries based on the ENDF/B-VII.0 data, fast system criticality benchmark problems [27,28] were analyzed using the MC^2-2 and TWODANT codes. Using the MC^2-2 code, 230-group cross sections were generated. Anisotropic scattering cross sections were generated up to Legendre order five. Anisotropic within-group scattering cross sections were modified to be consistent with the flux weighted total cross section to be used in the TWODANT code. The TWODANT calculations were performed with S_{24} angular quadrature and P_5 anisotropic scattering order. For comparison purposes, MC^2-2/TWODANT calculations for the fast system benchmark problems were repeated using the ENDF/B-V.2 and ENDF/B-VI.5 data.

Table 4.2 compares the multiplication factors obtained from ETOE-2/MC^2-2/TWODANT deterministic calculations with VIM or MCNP4C Monte Carlo results based on the ENDF/B-V.2 and ENDF/B-VI.5 data. In the case of ENDF/B-V.2 data, the TWODANT multiplication factors agree well with the VIM results within 170 pcm Δk, except for the FLATTOP and THOR benchmarks. For the FLATTOP and THOR benchmarks, the deviation of TWODANT k_{eff} value from VIM result is about 400 to 600 pcm Δk. These cores have a thick U-238 or Th-232 reflector, and the total amount of U-238 or Th-232 is more than 97 w/o of the total heavy metal mass. The neutron spectra of these cores are very hard, compared to the other cases as well as the ABTR numerical benchmark and the ZPPR-21 critical assemblies discussed in Sections 2 and 3. To identify the reason for relatively large discrepancy of deterministic solutions from Monte Carlo results, further investigation needs to be done.

For the ENDF/B-VI.5 data, the differences of multiplication factors between TWODANT and VIM are less than 290 pcm Δk in most cases, except for the FLATTOP-23 and THOR benchmarks. The FLATTOP-23 core uses U-233 as major fissile nuclides, and the THOR benchmark has a thick Th-232 reflector. Differences in the multiplication factor between VIM and MCNP4C Monte Carlo solutions are less than 100 pcm Δk except for ZPR6A and ZPR67. The difference between VIM and MCNP4C solutions is 190 pcm Δk for the ZPR6A problem and

-490 pcm Δk for the ZPR67 problem. Since these cores have a large amount of structure material, the consistency between VIM and MCNP4C cross section libraries for structural materials need to be reviewed.

Table 4.2 Comparison of Multiplication Factors of Fast System Benchmarks Obtained with ENDF/B-V.2 and ENDF/B-VI.5 Data

Fast System Benchmark	ENDF/B-V.2			ENDF/B-VI.5			
	VIM [a)]	E/M/T [b)]	Δk, pcm	VIM [a)]	E/M/T [b)]	Δk, pcm	MCNP4C [c)]
BIGTEN	1.00810	1.00649	-161	1.0094	1.00646	-290	1.0088
FLATTOP-25	1.00447	1.00858	411	1.0029	1.00547	260	1.0020
FLATTOP-PU	1.00332	1.00933	601	1.0038	1.00603	220	1.0036
FLATTOP-23	1.00070	1.00502	432	1.0010	1.00606	510	1.0001
GODIVA	0.99800	0.99778	-22	0.9974	1.00002	260	0.9969
JEZEBEL-PU	0.99911	0.99985	74	0.9990	1.00002	100	0.9997
JEZEBEL-23	0.99347	0.99295	-52	0.9937	0.99285	-90	0.9935
JEZEBEL	0.99743	0.99894	151	0.9978	0.99954	170	0.9969
ZPR6A	0.98050	0.98158	108	0.9997	0.99879	-90	0.9969
ZPR67	0.97860	0.97925	65	0.9884	0.98625	-220	0.9911
THOR	1.00564	1.01042	464	1.0064	1.01105	470	1.0074

a) Standard deviation of VIM < 0.0003
b) ETOE-2/MC^2-2/TWODANT ($S_{24}P_5$)
c) Standard deviation of MCNP4C < 0.0006

Table 4.3 compares the multiplication factors between the ETOE-2/MC^2-2/TWODANT deterministic calculations and the MCNP5 Monte Carlo calculations based on the ENDF/B-VII.0 data. As can be seen, the deviations of MC^2-2/TWODANT k_{eff} values from MCNP5 reference solutions are from -51 to 352 pcm Δk. Additional verification analyses are being performed for ZPR6A, ZPR67, and THOR critical experiments; the ZPR6A and ZPR67 benchmarks include a significant amount of structural materials and the THOR benchmark includes a large amount of Th-232, for which the problem was encountered in the multi-pole representation of Reich-Moore resonance parameters.

Table 4.3 Comparison of Multiplication Factors of Fast System Benchmarks Obtained with ENDF/B-VII.0 Data

Fast System Benchmark	ENDF/B-VII.0		
	MCNP5[a)]	E/M/T [b)]	Δk, pcm
BIGTEN	0.99161	0.99052	-51
FLATTOP-25	1.00212	1.00478	266
FLATTOP-PU	1.00072	1.00308	236
FLATTOP-23	0.99921	1.00257	336
GODIVA	0.99996	1.00348	352
JEZEBEL-PU	0.99944	1.00235	291
JEZEBEL-23	1.00007	1.00286	279
JEZEBEL	1.00028	1.00243	215
ZPR6A	0.99609	-	-
ZPR67	0.98671	-	-
THOR	0.99897	-	-

a) Standard deviation of MCNP4C < 0.00035
b) ETOE-2/MC^2-2/TWODANT ($S_{24}P_5$)

5. Conclusions

Validation studies of ANL neutronics analysis tools and nuclear data for Advanced Burner Reactor design applications have been initiated. As an initial effort, a numerical benchmark problem based on the reference metal fuel core concept of 250 MWt Advanced Burner Test Reactor (ABTR) and the six ZPPR-21 critical assemblies were analyzed. Preliminary tests of the ENDF/B-VII.0 data were also performed using a set of fast system criticality benchmark problems. Multi-group cross sections were generated using the ETOE-2/MC^2-2 codes based on the ENDF/B-V, ENDF/B-VI, and ENDF/B-VII nuclear data. For reference MCNP5 Monte Carlo calculations at elevated temperatures, MCNP cross section libraries were generated using the NJOY code. Deterministic core calculations were performed with the VARIANT nodal transport, TWODANT discrete ordinate transport, and DIF3D diffusion theory codes.

MCNP5 simulations for the ABTR numerical benchmark problem showed a significant dependence of Monte Carlo solutions on the base cross section libraries. The core multiplication factors determined with the ENDF/B-VI and VII data were different by almost 1.0 %Δk. Even different signs were observed among the sodium void worths obtained with different ENDF/B versions, although the sodium void worth of ABTR was estimated to be less than 1$. The control assembly worths predicted with different libraries showed a relative one standard deviation of 3%. The isothermal temperature coefficients predicted with the ENDF/B-VI and VII data showed about 3% difference, and the ENDF/B-V data yielded a 25% smaller coefficient in magnitude than the ENDF/B-VI and VII data. The local heterogeneity effect of fuel assembly was 0.30 %Δk; the duct heterogeneity effect was 0.25 %Δk and the fuel pin heterogeneity effect was only 0.05 %Δk. The control assembly heterogeneity effect was about 0.42 %Δk, and 0.40 %Δk was attributed to the duct heterogeneity.

Deterministic transport solutions of the ABTR benchmark obtained with 230-group VARIANT calculations showed good agreement with MCNP5 solutions. When all the control assemblies were out of the core, the difference in core multiplication factor was 0.21, -0.1, and 0.22 %Δk for the ENDF/B-V, VI, and VII libraries, respectively. When the control assemblies are fully inserted, this difference increased slightly, but still less than 0.36%. The sodium void worths agreed well with MCNP5 results, generally within 3-sigma Monte Carlo simulation uncertainty. The difference in control assembly worth between VARIANT and MCNP5 solutions was 0.8%, -2.3%, and -1.7% for the ENDF/B-V, VI, and VII libraries, respectively. The isothermal temperature coefficients agreed well with the MCNP5 results within about 2-sigma Monte Carlo simulation uncertainty. The assembly power distributions also agreed with the MCNP5 results within 3-sigma Monte Carlo statistical uncertainty.

When the number of energy groups was reduced from 230 to 33, the core multiplication factor was underestimated by almost 1.0%. However, the prediction accuracy for differential values such as sodium void worth and control assembly worth was deteriorated slightly. The ABTR benchmark problem showed a very large transport effect (~2 %Δk) because of its small

core size. The sodium void worth was also significantly underestimated by diffusion theory calculations. However, the control assembly worth and assembly power distribution were predicted very well with diffusion theory.

For all six ZPPR-21 configurations where the Pu-239 concentration varies from 0 to 49 w/o and the U-235 concentration accordingly varies from 62 to 0 w/o, the core multiplication factor determined with 230-group MC^2-2/TWODANT calculation based on the ENDF/B-V.2 data agreed with VIM Monte Carlo solution within 0.20 %Δk and there was no indication of any systematic bias. The quality of principal cross sections generated with the MC^2-2 code was comparable to that of VIM cross sections. The overall reactivity effect due to the errors in 230-group principal cross sections was estimated to be less than 0.05 %Δk for the ZPPR-21 critical assemblies. The statistics of the differences between calculated values and specified benchmark values showed similar bias and uncertainty for MC^2-2/TWODANT and VIM. This result suggests that the criticality prediction accuracy of MC^2-2/TWODANT is comparable to VIM.

Investigation of group collapsing methods showed that direct generation of broad-group cross sections from MC^2-2 calculations was not adequate for analysis of ZPPR-21 assemblies. Scalar flux weighting for all cross sections including anisotropic cross sections was not sufficiently accurate, either. The use of higher flux moments for anisotropic scattering cross section collapsing reproduced the fine-group results with broad-group cross sections.

Additional preliminary tests of the ENDF/B-VII.0 data were also performed using a set of fast system criticality benchmark problems. The ETOE-2 code was modified to treat the changes made in the ENDF/B-VII data. Several code modifications were made on the ETOE-2 code. Important isotopes pertinent to the ABTR benchmark and fast system criticality benchmark problems were successfully processed into the MC^2-2 library formats. A few isotopes which could not be processed correctly with the multi-pole representation option were processed with the Adler-Adler representation option. The verification results with fast system criticality benchmark problems showed that the multiplication factors of MC^2-2/TWODANT agreed with MCNP5 results within 0.35 %Δk for the cases analyzed successfully. However, the cases with U-233 and Th-232 were not successfully analyzed yet.

In conclusion, the ANL suite of deterministic neutronics analysis tools appears to be adequate to use in the initial design stage of Advanced Burner Reactors, of which startup fuel is expected to be conventional plutonium fuel. However, further verification/validation studies need to be performed for transmutation fuel to assess the impact of relatively large amount of minor actinides. In addition, the ETOE-2/MC^2-2 system for multi-group cross section generation needs to be thoroughly tested to process the new ENDF/B-VII data. Several improvements are also highly desirable, including the capability to handle all the ENDF formats for secondary particle energy and angular distributions, proper treatment of fission spectrum dependence on incident neutron energy, and enhanced resonance screening procedures.

References

1. L. G. Lesage, "An Overview of the Argonne National Laboratory Fast Critical Experiments 1963-1990," ANL-NT-175, Argonne National Laboratory, April 2001.
2. H. F. McFarlane, "The Use of Critical Experiments in CRBR Design: Status and Historical Perspective," ANL-80-119, Argonne National Laboratory, November 1980.
3. L. G. LeSage, M. J. Lineberry, and H. F. McFarlane, "Current Status of Fast Reactor Physics Reactivity Coefficients," *Progress in Nuclear Energy*, **16**, 231 (1985).
4. M. J. Lineberry, H. F. McFarlane, and P. J. Collins, "Physics Assessments of LMFBR Integral Parameters," *Proc. of the Topical Meeting on Advances in Reactor Physics and Core Thermal Hydraulics*, Kiamesha Lake, New York, Sept. 22-24, 1982, NUREG/CP-0034, Vol. 1, p. 1-19 (1982).
5. "Application of Critical Experiments and Operating Data to Core Design Via Formal Methods of Cross Section Data Adjustment," *Proc of the NEACRP Specialists Meeting*, Jackson Hole, Wyoming, Sept. 23-24, 1988, NEACRP-L-307.
6. D. C. Wade, "Monte Carlo-based Validation of the ENDF/MC^2-II/SDX Cell Homogenization Path," ANL-79-5, Argonne National Laboratory, April 1979.
7. R. D. McKnight and J. R. Krsul, "Validation Results Based on the Spent Fuel Demonstration Program at FCF," *Proc. ANS Fourth Topical Meeting on DOE Spent Nuclear Fuel and Fissile Material Management*, San Diego, CA, June 4-8, 2000.
8. R. D. McKnight, "ANL Calculational Methodologies for Determining Spent Nuclear Fuel Source Term," *Proc. ANS Fourth Topical Meeting on DOE Spent Nuclear Fuel and Fissile Material Management*, San Diego, CA, June 4-8, 2000.
9. P. Oblozinsky and M. Herman, "Special Issues on Evaluated Nuclear Data File ENDF/B-VII.0," *Nuclear Data Sheets*, **107**, 2931 (2006).
10. Y. I. Chang, et al., "Advanced Burner Test Reactor Preconceptual Design Report," ANL-ABR-1, Argonne National Laboratory, September 2006.
11. B. J. Toppel, H. Henryson II, and C. G. Stenberg, "ETOR-2/MC^2-2/SDX Multigroup Cross-Section Processing," Conf-780334-5, Presentation at RSIC Seminar Workshop on Multigroup Cross Sections, Oak Ridge, TN (March 1978)
12. H. Henryson II, B. J. Toppel, and C. G. Stenberg, "MC^2-2: A Code to Calculate Fast Neutron Spectra and Multigroup Cross Sections," FRA-TM-89, Argonne National Laboratory (1976).
13. G. C. Palmiotti, E. E. Lewis, and C. B. Carrico, "VARIANT: Variational Anisotropic Nodal Transport for Multidimensional Cartesian and Hexagonal Geometry Calculation," ANL-95/40, Argonne National Laboratory (1995).
14. Derstine, K. L., "DIF3D: A Code to Solve One-, Two-, and Three-Dimensional Diffusion Theory Problems," ANL-82-64, Argonne National Laboratory, (1982).
15. R. D. Lawrence, "The DIF3D Nodal Neutronics Option for Two- and Three-Dimensional Diffusion Theory Calculations in Hexagonal Geometry," ANL-83-1, Argonne National Laboratory (1983).

16. "MCNP – A General Monte Carlo N-Particle Transport Code," Version 5, LA-UR-03-1987, Los Alamos National Laboratory (April 24, 2003).

17. MacFarlane, R. E., "NJOY 99/2001: New Capabilities in Data Processing," Presentation at the Workshop on Reactor Physics and Analysis Capabilities for Generation IV Nuclear Energy Systems, Argonne National Laboratory, Argonne, Illinois, February 18-19, (2003).

18. Alcouffe, R. E., Brinkley, F. W., Marr, D. R., and O'Dell, R. D., "User's Guide for TWODANT: A Code Package for Two-Dimensional, Diffusion-Accelerated, Neutral-Particle Transport," LA-10049-M, Los Alamos National Laboratory (1990).

19. R. M. Lell, R. W. Schaefer, R. D. McKnight, and A. Mohamed, "ZPPR-21 Phase A: A Cylindrical Assembly of Pu Metal Reflected by Graphite," PU-MET-FAST-033, OECD/NEA, International Handbook of Evaluated Criticality Safety Benchmark Experiments, NEA/NSC/DOC(95)03 (2005).

20. R. D. McKnight, R. M. Lell, R. W. Schaefer, and A. Mohamed, "ZPPR-21 Phases B through E: Cylindrical Assemblies of Mixed Fissile Pu and U Metal Reflected by Graphite," MIX-MET-FAST-011, OECD/NEA, International Handbook of Evaluated Criticality Safety Benchmark Experiments, NEA/NSC/DOC(95)03 (2005).

21. R. W. Schaefer, R. D. McKnight, R. M. Lell, and A. Mohamed, "ZPPR-21 Phase F: A Cylindrical Assembly of U Metal Reflected by Graphite," HEU-MET-FAST-061, OECD/NEA, International Handbook of Evaluated Criticality Safety Benchmark Experiments, NEA/NSC/DOC(95)03 (2005).

22. R. N. Blomquist, "VIM Continuous Energy Monte Carlo Transport Code," *Proc. Intl. Conf. on Mathematics, Computations, Reactor Physics and Environmental Analysis,* Portland, OR, April 30-May 4, 1995.

23. R. N. Hwang, "A Rigorous Pole Representation of Multilevel Cross Sections and Its Practical Applications," *Nucl. Sci. Eng.*, **96**, 192 (1987).

24. E. E. Lewis and W. F. Miller, Jr., *Computational Methods of Neutron Transport*, John Wiley and Sons, New York (1984).

25. R. N. Hwang, Private Communication, Argonne National Laboratory. August 2002.

26. R. N. Hwang, B. J. Toppel, and H. Henryson II, "Improved Algorithms for the Calculation of Resolved Resonance Cross Sections with Application to the Structural Doppler Effect," ANL-80-104, Argonne National Laboratory, October 1980.

27. C. Stenberg, R. McKnight, "Verification and Validation of Fast Systems with ENDF/B Data," ANS Nuclear Criticality Safety Division Embedded Topical Meeting, Reno, Nevada, Nov. 11-15 (2001).

28. NEA Nuclear Science Committee, "International Handbook of Evaluated Criticality Safety Benchmark Experiments," NEA/NSC/DOC(95)03 (September 2006).

Appendix A. ABTR Numerical Benchmark Problem

Based on the reference 250 MWt ABTR metal core design fueled with weapons-grade plutonium feed, a numerical benchmark problem was developed with fuel compositions at the beginning of equilibrium cycle. Three fuel compositions were derived by averaging the detailed spatial distributions of isotopic number densities determined from an equilibrium cycle analysis over the inner core, outer core, and fuel test assemblies. The geometries and material densities at the assumed operating conditions were used. The temperatures and thermal expansions at the operating conditions are provided in Table A.1. The material thermal expansion was modeled by adjusting the hexagonal pitch, axial meshes, and fuel and structure material densities appropriately. For simplicity, the wire wrap was smeared with the cladding, and the gap between B_4C pellet and cladding was neglected in the control and shield assemblies. It was also assumed that due to irradiation swelling, the fuel slug is contact with the cladding and the bond sodium is displaced into the lower part of fission gas plenum. To facilitate Monte Carlo simulation, all the fission products were replaced with molybdenum.

Table A.1 Assumed Temperature and Thermal Expansion Data at Operating Condition

Temperature (°C)	Coolant in active core	432.5
	Cladding	462.5
	Fuel	582.5
	Reflector	432.5
	Shield	355.0
	Lower structure and reflector	355.0
	Upper plenum and structure	510.0
Expansion (%)	Radial expansion	0.596
	Axial expansion	0.489
	Fuel irradiation axial swelling	5.0
	Axial expansion of control rod absorber	0.540

The design parameters of fuel, reflector, shield and control assemblies are presented in Tables A.2 to A.5, respectively. For comparison, dimensions at both cold and hot conditions are provided in these tables. The fuel assembly contains 217 fuel pins arranged in a triangular pitch array. The reflector assembly contains 91 solid HT-9 pins arranged in a triangular pitch array. The shield assembly consists of 19 thick HT-9 tubes containing boron carbide pellets. The natural boron (B-10 abundance of 19.9 atomic percent) is used with 81% of a smeared B_4C pellet density. The control assemblies consist of an absorber bundle contained within a duct. The absorber bundle is a closely packed array of tubes containing compacted boron carbide pellets. The bundle of pins is contained in an interior duct that channels flow through the bundle and

protects the pins from damage as they slide within the outer fixed duct. The outer duct of the control rod assembly has the same external dimensions as the fuel assembly duct.

Figures A.1 to A.3 show the schematics of fuel, control, and reflector/shield assemblies, respectively. Dimensions are given at the operating conditions. For simplicity, the lower and upper structures of all the assemblies are modeled as a homogenized mixture of coolant (70 volume %) and structural materials (30 volume %).

Nuclide atomic densities of heterogeneous and homogenized assembly models are provided in Tables A.6 to A.17 for different axial segments of every assembly type. For the heterogeneous assembly models, the nuclide number densities are given separately for each material in the assembly. For example, in the active core segment of fuel assembly, the nuclide densities are separately provided for fuel slug, cladding, coolant, and assembly duct. For the homogenized assembly model, the nuclide densities are homogenized values over the assembly pitch (including the inter-assembly gap) in the radial direction and over the corresponding axial segment in the axial direction.

Table A.2 Parameters of Fuel Assembly

	Cold	Hot
Overall length of duct, cm	340.000	341.663
Number of pins	217	
Smeared density, %	75	
Fuel pin pitch, cm	0.9080	0.9134
Fuel pin diameter, cm	0.8000	0.8048
Thickness of clad, cm	0.0520	0.0523
Outer radius of clad, cm	0.4000	0.4024
Inner radius of clad, cm	0.3480	0.3501
Fuel slug radius, cm	0.3014	0.3501
Active core height, cm	80.0000	84.4108
Gas plenum height, cm	120.0000	120.5868
Assembly pitch, cm	14.5980	14.6850
Duct outer Flat-to-Flat distance, cm	14.1980	14.2826
Duct wall thickness, cm	0.3000	0.3018
Duct inside flat-to-flat distance, cm	13.5980	13.6790
Wire wrap radius, cm	0.0515	
Wire wrap axial pitch, cm	20.3200	
Clad outer radius including wire-wrap, cm		0.4057
Lower reflector height, cm	60.000	60.293
length of displaced sodium bond, cm	0.0000	19.7637

Table A.3 Parameters of Reflector Assembly

	Cold	Hot
Overall length of duct, cm	340.000	341.663
Number of pins	91	
Pin pitch, cm	1.4067	1.4151
Reflector rod diameter, cm	1.4052	1.4136
Reflector rod radius, cm	0.7026	0.7068
Reflector rod height, cm	260.0000	261.2714
Assembly pitch, cm	14.5980	14.6850
Duct outer flat-to-flat distance, cm	14.1980	14.2826
Duct wall thickness, cm	0.3000	0.3018
Duct inside flat-to-flat distance, cm	13.5980	13.6790

Table A.4 Parameters of Shield Assembly

	Cold	Hot
Overall length of duct, cm	340.000	341.663
Number of pins	19	
Absorber smear density, %	81	
Shield pin pitch, cm	3.0441	3.0622
Shield pin diameter, cm	3.0426	3.0607
Thickness of clad, cm	0.2500	0.2515
Outer radius of clad, cm	1.5213	1.5304
Inner radius of clad, cm	1.2713	1.2789
Absorber radius, cm	1.1442	1.2789
Absorber height, cm	260.0000	261.2714
Assembly pitch, cm	14.5980	14.6850
Duct outer flat-to-flat distance, cm	14.1980	14.2826
Duct wall thickness, cm	0.3000	0.3018
Duct inside flat-to-flat distance, cm	13.5980	13.6790

Table A.5 Parameters of Control Assembly

	Cold	Hot
Overall length of duct, cm	340.000	341.663
Number of pins	91	
Absorber smear density, %	81	
Rod pitch, cm	1.2484	1.2558
pin diameter, cm	1.1104	1.1170
Thickness of clad, cm	0.0700	0.0704
Outer radius of clad, cm	0.5552	0.5585
Inner radius of clad, cm	0.4852	0.4881
Absorber radius, cm	0.4473	0.4881
Absorber height, cm	85.0000	85.4157
Assembly pitch, cm	14.5980	14.6850
Duct outer flat-to-flat distance, cm	14.1980	14.2826
Duct wall thickness, cm	0.3000	0.3018
Duct inside flat-to-flat distance, cm	13.5980	13.6790
Inner duct outer flat-to-flat distance, cm	12.7980	12.8743
Inner duct inner flat-to-flat distance, cm	12.1980	12.2707
Wire wrap radius, cm	0.0665	
Wire wrap axial pitch, cm	20.3200	
Clad outer radius with wire-wrap, cm		0.5626
Radius of follower, cm	5.0000	5.0298
Length of follower, cm	16.8000	16.8822

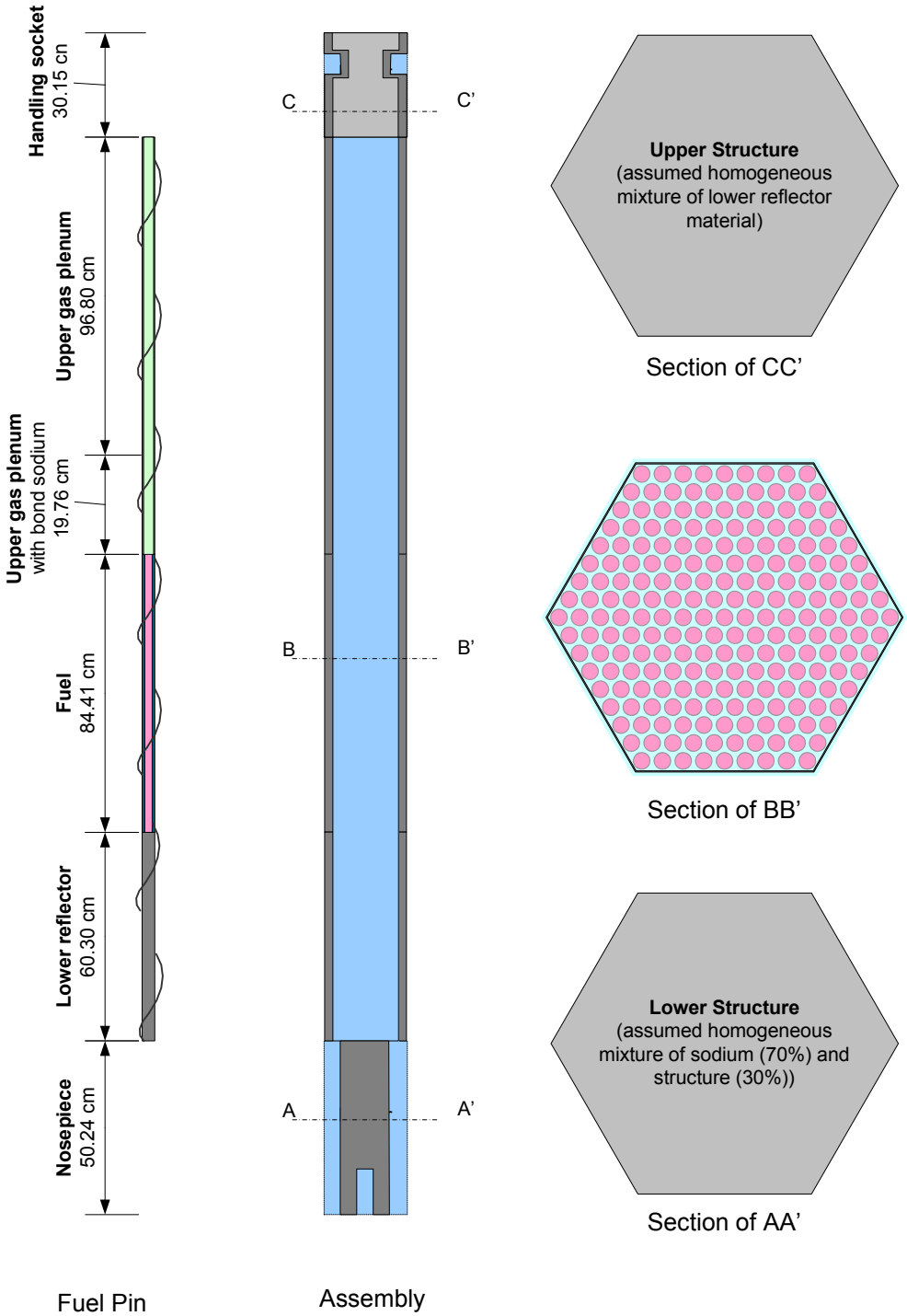

Figure A.1 Fuel Assembly Schematics

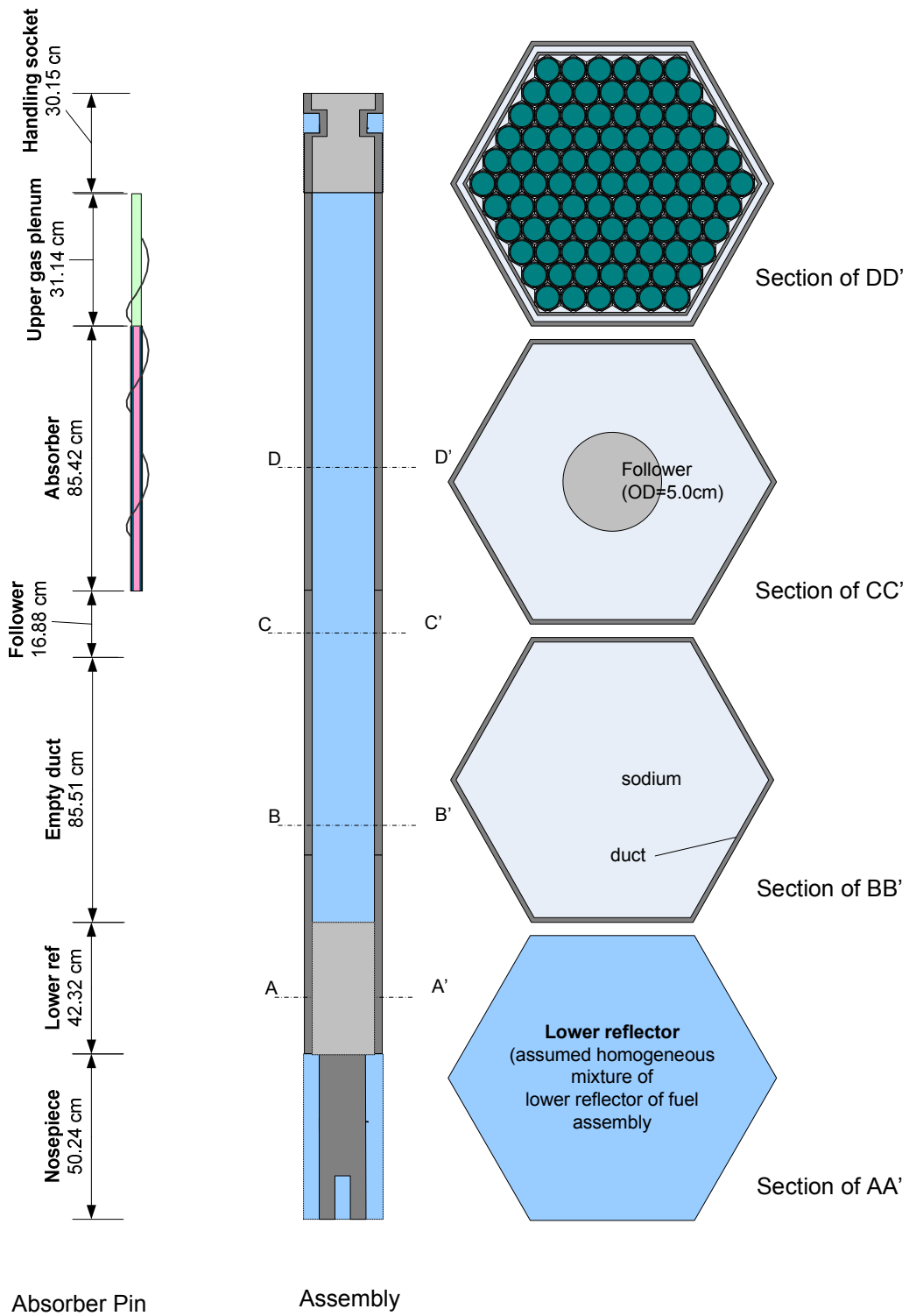

Figure A.2 Control Assembly Schematics

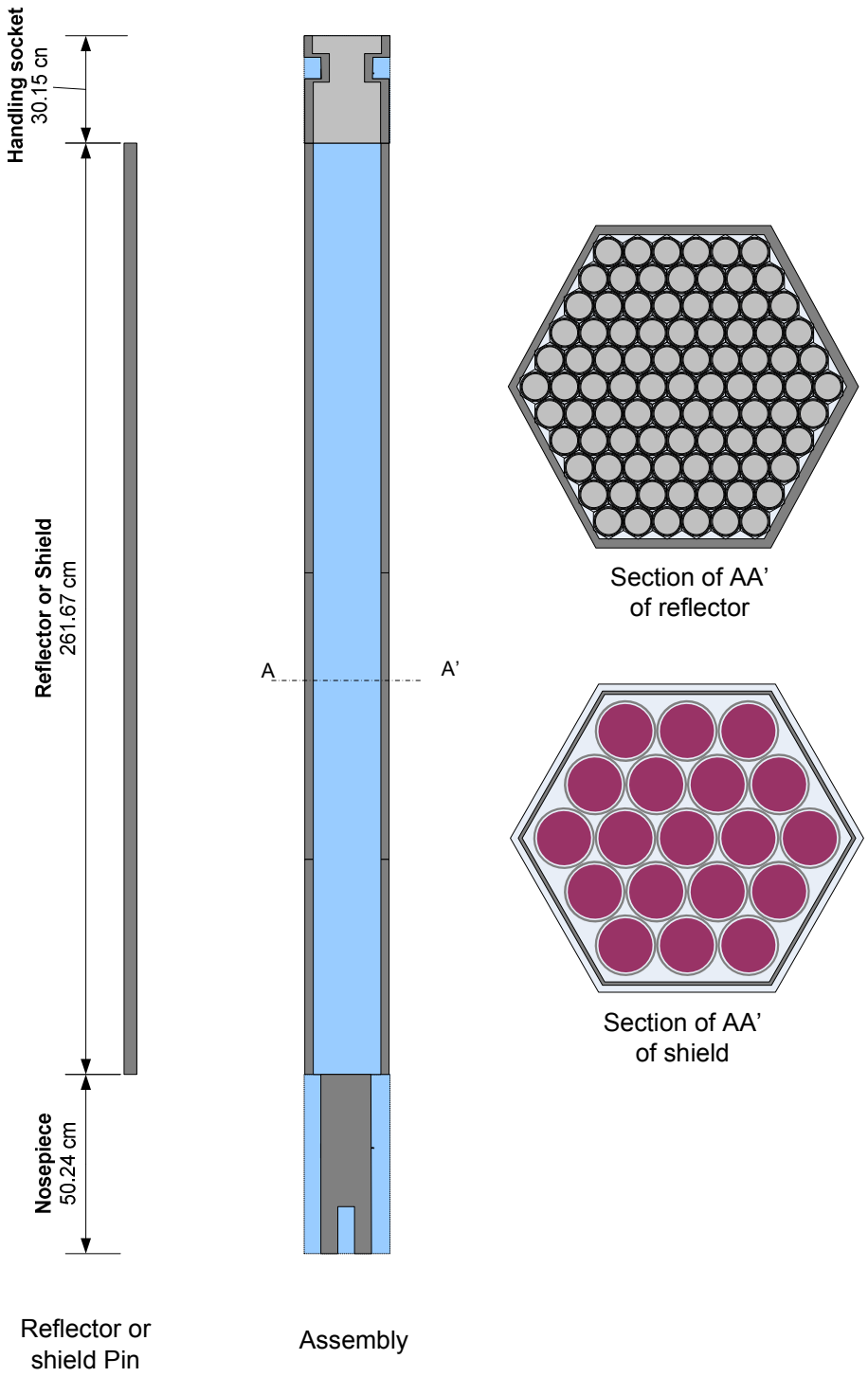

Figure A.3 Radial Reflector/Shield Assembly Schematics

Table A.6 Nuclide Densities of Lower Reflector of Fuel Assembly

Nuclide	Heterogeneous assembly			Homogenized assembly
	HT-9 pin	Coolant	Duct	
Na		2.2272E-02		7.1455E-03
Fe	6.9844E-02		6.9844E-02	4.7436E-02
Ni	4.3063E-04		4.3063E-04	2.9248E-04
Cr	1.0385E-02		1.0385E-02	7.0532E-03
Mn55	4.6007E-04		4.6007E-04	3.1247E-04
Mo	4.9097E-04		4.9097E-04	3.3346E-04

Table A.7 Nuclide Densities of Active Core Section of Fuel Assembly

Nuclide	Heterogeneous fuel			Cladding	Coolant	Duct
	inner core	fuel test	out core	HT9	Sodium	HT9
U-234	1.2225E-08	1.0027E-06	1.4997E-08			
U-235	3.2248E-05	3.2038E-05	3.1767E-05			
U-236	2.0561E-06	1.9484E-06	1.8593E-06			
U-238	2.0222E-02	1.9745E-02	1.9317E-02			
Np237	3.8387E-06	1.8093E-04	3.1274E-06			
Pu236	1.3918E-11	9.0759E-10	9.1074E-12			
Pu238	9.5854E-07	9.0509E-05	9.8743E-07			
Pu239	3.4991E-03	2.3546E-03	4.3068E-03			
Pu240	3.7398E-04	1.0881E-03	4.5617E-04			
Pu241	2.4535E-05	2.9432E-04	2.9545E-05			
Pu242	1.7542E-06	2.1919E-04	2.0615E-06			
Am241	1.4209E-06	2.1306E-04	2.2274E-06			
Am242m	2.8475E-08	5.8336E-06	4.0761E-08			
Am243	6.1338E-08	4.3624E-05	7.5588E-08			
Cm242	4.7083E-08	7.3545E-06	5.6294E-08			
Cm243	7.4138E-10	2.4428E-07	9.0540E-10			
Cm244	4.8305E-09	1.0986E-05	5.5302E-09			
Cm245	1.9064E-10	9.7716E-07	1.9972E-10			
Cm246	2.6112E-12	6.7680E-08	2.4070E-12			
Zr	7.2938E-03	7.2938E-03	7.2938E-03			
Na					2.2272E-02	
Fe				6.9844E-02		6.9844E-02
Ni				4.3063E-04		4.3063E-04
Cr				1.0385E-02		1.0385E-02
Mn55				4.6007E-04		4.6007E-04
Mo	9.76123E-04	8.36399E-04	9.81845E-04	4.9097E-04		4.9097E-04

Table A.7 Nuclide Densities of Active Core Section of Fuel Assembly (cont'd)

Nuclide	Homogenized assembly model		
	Inner core	fuel test	outer core
U-234	5.46898E-09	4.48578E-07	6.70877E-09
U-235	1.44262E-05	1.43324E-05	1.42111E-05
U-236	9.19798E-07	8.71638E-07	8.31760E-07
U-238	9.04638E-03	8.83280E-03	8.64147E-03
Np237	1.71727E-06	8.09410E-05	1.39907E-06
Pu236	6.22636E-12	4.06014E-10	4.07421E-12
Pu238	4.28807E-07	4.04893E-05	4.41730E-07
Pu239	1.56532E-03	1.05336E-03	1.92666E-03
Pu240	1.67301E-04	4.86743E-04	2.04069E-04
Pu241	1.09760E-05	1.31667E-04	1.32172E-05
Pu242	7.84751E-07	9.80540E-05	9.22204E-07
Am241	6.35636E-07	9.53142E-05	9.96453E-07
Am242m	1.27384E-08	2.60969E-06	1.82346E-08
Am243	2.74399E-08	1.95154E-05	3.38145E-08
Cm242	2.10628E-08	3.29008E-06	2.51831E-08
Cm243	3.31661E-10	1.09281E-07	4.05034E-10
Cm244	2.16096E-09	4.91452E-06	2.47394E-09
Cm245	8.52838E-11	4.37138E-07	8.93442E-11
Cm246	1.16811E-12	3.02767E-08	1.07680E-12
Zr	3.26289E-03	3.26289E-03	3.26289E-03
Na	7.14528E-03	7.14528E-03	7.14528E-03
Fe	1.61921E-02	1.61921E-02	1.61921E-02
Ni	9.98349E-05	9.98349E-05	9.98349E-05
Cr	2.40756E-03	2.40756E-03	2.40756E-03
Mn55	1.06659E-04	1.06659E-04	1.06659E-04
Mo	5.50492E-04	4.87986E-04	5.53051E-04

- Na density of voided homogenized model is 1.2039E-3

Table A.8 Nuclide Densities of Gas plenum of Fuel Assembly (Lower Part with Na Bond)

Nuclide	Heterogeneous assembly			Homogenized assembly
	Cladding	Coolant	Duct	
Na		2.2272E-02		1.7109E-02
Fe	6.9844E-02		6.9844E-02	1.6192E-02
Ni	4.3063E-04		4.3063E-04	9.9831E-05
Cr	1.0385E-02		1.0385E-02	2.4075E-03
Mn55	4.6007E-04		4.6007E-04	1.0666E-04
Mo	4.9097E-04		4.9097E-04	1.1382E-04

- Na density of voided homogenized model is 1.1167E-2

Table A.9 Nuclide Densities of Gas plenum of Fuel Assembly (Upper Part)

Nuclide	Heterogeneous assembly			Homogenized assembly
	Cladding	Coolant	Duct	
Na		2.2272E-02		7.1455E-03
Fe	6.9844E-02		6.9844E-02	1.6192E-02
Ni	4.3063E-04		4.3063E-04	9.9831E-05
Cr	1.0385E-02		1.0385E-02	2.4075E-03
Mn55	4.6007E-04		4.6007E-04	1.0666E-04
Mo	4.9097E-04		4.9097E-04	1.1382E-04

- Na density of homogenized voided case is 1.2039E-3

Table A.10 Nuclide Densities of Sodium-Filled Part under Control Rod

Nuclide	Heterogeneous assembly		Homogenized assembly
	Coolant	Duct	
Na	2.2272E-02		2.0529E-02
Fe		6.9844E-02	5.4661E-03
Ni		4.3063E-04	3.3702E-05
Cr		1.0385E-02	8.1273E-04
Mn55		4.6007E-04	3.6006E-05
Mo		4.9097E-04	3.8424E-05

Table A.11 Nuclide Densities of Control Rod Follower

Nuclide	Heterogeneous assembly			Homogenized assembly
	Follower	Coolant	Duct	
Na		2.22724E-02		1.1051E-02
Fe	5.2048E-02		6.9844E-02	2.7616E-02
Ni	1.0687E-02		4.3063E-04	4.5819E-03
Cr	1.0606E-02		1.0385E-02	5.3263E-03
Mn55	1.6667E-03		4.6007E-04	7.4530E-04
Mo	1.4267E-03		4.9097E-04	6.4558E-04

Table A.12 Nuclide Densities of Control Rod

Nuclide	Heterogeneous assembly				Homogenized assembly
	Absorber	Cladding	Coolant	Duct	
C	4.0679E-03				1.4834E-03
B10	1.6441E-02				5.9956E-03
B11	6.6179E-02				2.4133E-02
Na			2.2272E-02		8.1722E-03
Fe		6.9844E-02		6.9844E-02	1.8747E-02
Ni		4.3063E-04		4.3063E-04	1.1559E-04
Cr		1.0385E-02		1.0385E-02	2.7875E-03
Mn55		4.6007E-04		4.6007E-04	1.2349E-04
Mo		4.9097E-04		4.9097E-04	1.3179E-04

Table A.13 Nuclide Densities of Gas Plenum of Control Rod

Nuclide	Heterogeneous assembly			Homogenized assembly
	Cladding	Coolant	Duct	
Na		2.2272E-02		8.1722E-03
Fe	6.9844E-02		6.9844E-02	1.8747E-02
Ni	4.3063E-04		4.3063E-04	1.1559E-04
Cr	1.0385E-02		1.0385E-02	2.7875E-03
Mn55	4.6007E-04		4.6007E-04	1.2349E-04
Mo	4.9097E-04		4.9097E-04	1.3179E-04

Table A.14 Nuclide Densities of Reflector

Nuclide	Heterogeneous assembly			Homogenized assembly
	HT-9 rod	Coolant	Duct	
Na		2.2272E-02		3.4976E-03
Fe	6.9844E-02		6.9844E-02	5.8876E-02
Ni	4.3063E-04		4.3063E-04	3.6301E-04
Cr	1.0385E-02		1.0385E-02	8.7541E-03
Mn55	4.6007E-04		4.6007E-04	3.8782E-04
Mo	4.9097E-04		4.9097E-04	4.1387E-04

Table A.15 Nuclide Densities of Shield

Nuclide	Heterogeneous assembly				Homogenized assembly
	Absorber	Cladding	Coolant	Duct	
C	3.7154E-03				1.9422E-03
B10	1.5668E-02				8.1900E-03
B11	6.3065E-02				3.2966E-02
Na			2.2272E-02		3.8576E-03
Fe		6.9844E-02		6.9844E-02	2.1237E-02
Ni		4.3063E-04		4.3063E-04	1.3094E-04
Cr		1.0385E-02		1.0385E-02	3.1577E-03
Mn55		4.6007E-04		4.6007E-04	1.3989E-04
Mo		4.9097E-04		4.9097E-04	1.4929E-04

Table A.16 Nuclide Densities of Core Barrel and Coolant

Nuclide	Heterogeneous assembly		Homogenized assembly
	Barrel	Coolant	
Na		2.22724E-02	1.81469E-02
Fe	5.20478E-02		9.64075E-03
Ni	1.06872E-02		1.97959E-03
Cr	1.06058E-02		1.96450E-03
Mn55	1.66670E-03		3.08720E-04
Mo	1.42668E-03		2.64263E-04

Table A.17 Nuclide Densities of Lower and Upper Structures

Nuclide	Heterogeneous and homogenized assembly models
Na	1.5591E-02
Fe	1.5878E-02
Ni	3.2604E-03
Cr	3.2355E-03
Mn55	5.0846E-04
Mo	4.3524E-04

Nuclear Engineering Division
Argonne National Laboratory
9700 South Cass Avenue
Argonne, IL 60439

www.anl.gov

Argonne National Laboratory is a U.S. Department of Energy
laboratory managed by UChicago Argonne, LLC